

Investigation of Aerodynamic Interference of Double Deck Bridges.

May 2016

About Argonne National Laboratory

Argonne is a U.S. Department of Energy laboratory managed by UChicago Argonne, LLC under contract DE-AC02-06CH11357. The Laboratory's main facility is outside Chicago, at 9700 South Cass Avenue, Argonne, Illinois 60439. For information about Argonne and its pioneering science and technology programs, see www.anl.gov.

DOCUMENT AVAILABILITY

Online Access: U.S. Department of Energy (DOE) reports produced after 1991 and a growing number of pre-1991 documents are available free via DOE's SciTech Connect (<http://www.osti.gov/scitech/>)

Reports not in digital format may be purchased by the public from the National Technical Information Service (NTIS):

U.S. Department of Commerce
National Technical Information Service
5301 Shawnee Rd
Alexandria, VA 22312
www.ntis.gov
Phone: (800) 553-NTIS (6847) or (703) 605-6000
Fax: (703) 605-6900
Email: orders@ntis.gov

Reports not in digital format are available to DOE and DOE contractors from the Office of Scientific and Technical Information (OSTI):

U.S. Department of Energy
Office of Scientific and Technical Information
P.O. Box 62
Oak Ridge, TN 37831-0062
www.osti.gov
Phone: (865) 576-8401
Fax: (865) 576-5728
Email: reports@osti.gov

Disclaimer

This report was prepared as an account of work sponsored by an agency of the United States Government. Neither the United States Government nor any agency thereof, nor UChicago Argonne, LLC, nor any of their employees or officers, makes any warranty, express or implied, or assumes any legal liability or responsibility for the accuracy, completeness, or usefulness of any information, apparatus, product, or process disclosed, or represents that its use would not infringe privately owned rights. Reference herein to any specific commercial product, process, or service by trade name, trademark, manufacturer, or otherwise, does not necessarily constitute or imply its endorsement, recommendation, or favoring by the United States Government or any agency thereof. The views and opinions of document authors expressed herein do not necessarily state or reflect those of the United States Government or any agency thereof, Argonne National Laboratory, or UChicago Argonne, LLC.

Investigation of Aerodynamic Interference of Double Deck Bridges.

by

M.A. Sitek, C. Bojanowski, and S.A. Lottes

Transportation Research and Analysis Computing Center (TRACC)

Energy Systems Division, Argonne National Laboratory

May 2016

Table of Contents

1. Introduction	1
1.1. Motivation.....	1
1.2. Proposed analysis methods	3
2. CFD model.....	3
2.1. General information	3
2.2. Mesh study.....	5
2.3. Pressure and velocity fields with a single deck.....	9
3. Analysis of double deck bridges	16
3.1. Pressure and velocity fields on double decks.....	16
3.2. Varying horizontal gap between decks	26
3.3. Varying angle of attack	31
3.4. LES turbulence modeling	37
4. Dynamic response	39
4.1. Configuration 1: both decks are suspended on springs	39
4.2. Configuration 2: deck 1 is suspended on springs and deck 2 is constrained.....	49
4.3. Configuration 3: deck 1 is constrained and deck 2 is suspended on springs.....	50
4.4. Comparison of results for configurations 1, 2, and 3.....	51
5. Conclusions	54
6. References	56

List of Figures

Figure 1.1: Thaddeus Kosciusko Bridge, NY, by Njhepler at English Wikipedia, CC BY 2.5, https://commons.wikimedia.org/w/index.php?curid=12452015	2
Figure 1.2: Fred Hartman Bridge, TX, by United States Coast Guard, PA2 James Dillard - U.S. Coast Guard Visual Information GalleryU.S. Coast Guard Visual Information Gallery Home, Public Domain, https://commons.wikimedia.org/w/index.php?curid=3499375	2
Figure 2.1: The computational domain.....	4
Figure 2.2: An example mesh around single and double deck cross sections.....	4
Figure 2.3: Force component values vs. wall Y^+	6
Figure 2.4: Moment component values vs. Y^+	7
Figure 2.5: Mesh influence on force and moment components values acting on deck 1	8
Figure 2.6: Mesh influence on force and moment components values acting on deck 2.....	9
Figure 2.7: Single deck. Pressure plot on the mid surface of the domain a) general view, b) the area around the deck.....	10
Figure 2.8: Single deck. Horizontal velocity plot on the mid surface of the domain a) general view, b) the area around the deck.....	11
Figure 3.1: Pressure contour plot around the decks, a) URANS, b) LES, polyhedral mesh, $Y^+=117$	
Figure 3.2: Pressure on the symmetry line of the top surface of deck 1, a) location of measured points, b) pressure values	18
Figure 3.3: Pressure on the symmetry line of the bottom surface of deck 1, a) location of measured points, b) pressure values	19
Figure 3.4: Pressure on the symmetry line of the top surface of deck 2, a) location of measured points, b) pressure values	20
Figure 3.5: Pressure on the symmetry line of the bottom surface of deck 2, a) location of measured points, b) pressure values	21
Figure 3.6: Pressure on the symmetry line of the upwind surface of deck 1, a) location of measured points, b) pressure values	22
Figure 3.7: Pressure on the symmetry line of the downwind surface of deck 1, a) location of measured points, b) pressure values	23

Figure 3.8: Pressure on the symmetry line of the upwind surface of deck 2, a) location of measured points, b) pressure values	24
Figure 3.9: Pressure on the symmetry line of the downwind surface of deck 2, a) location of measured points, b) pressure values	25
Figure 3.10: Gap influence on the drag force at parallel flow.....	30
Figure 3.11: Gap influence on the lift force at parallel flow	30
Figure 3.12: Gap influence on the pitch moment at parallel flow	30
Figure 3.13: Influence of angle of attack on drag force, gap=0.1 m	36
Figure 3.14: Influence of angle of attack on lift force, gap=0.1 m	36
Figure 3.15: Influence of angle of attack on pitch moment, gap=0.1 m	36
Figure 4.1: Double deck model on elastic springs	40
Figure 4.2: Vertical translations of the decks in time, a) during the entire simulation, b) during last 10 seconds of the simulation time.....	41
Figure 4.3: Vibration frequencies of the decks	42
Figure 4.4: Rotations of the decks in time, a) during the entire simulation, b) during last 10 seconds of the simulation time	43
Figure 4.5: Forces acting on the decks in configuration 1, a) drag, b) lift and c) moment.....	44
Figure 4.6: Forces acting on the decks in configuration 2, a) drag force, b) lift force, c) moment.	50
Figure 4.7: Forces acting on the decks in configuration 3, a) drag force, b) lift force, c) moment.....	51
Figure 4.8: Comparison of force values acting on deck 1 at different configurations	52
Figure 4.9: Comparison of force values acting on deck 2 at different configurations.....	53

List of Tables

Table 1: Types of meshes used in the simulations	5
Table 2: Pressure field contour plots for a single deck bridge at varying angle of attack	12
Table 3: Velocity field contour plots for a single deck bridge at varying angle of attack	14
Table 4: Extreme values of pressure and velocity for a single deck	16
Table 5: Extreme values of pressure and velocity for a double deck with varying gap	26
Table 6: Pressure and velocity fields around double deck with varying gap	26
Table 7: Velocity field contour plots for a single deck bridge at varying gap	28
Table 8: Pressure field contour plots for a double deck bridge with gap 0.1 m at varying angle of attack.....	31
Table 9: Velocity field contour plots for a double deck bridge with gap 0.1 m at varying angle of attack.....	33
Table 10: Extreme values of pressure and velocity for a double deck	35
Table 11: The change in time of velocity vector field around the decks on a plane section.....	37
Table 12: Velocity vector field on the middle plane in consecutive time steps.....	45
Table 13: Velocity streamlines in consecutive time steps	47

1. Introduction

1.1. Motivation

Construction of a twin bridge can be a cost effective and minimally disruptive way to increase capacity when an existing bridge is not near the end of its service life. With ever growing vehicular traffic, when demand approaches the capacity of many existing roads and bridges. Remodeling a structure with an insufficient number of lanes can be a good solution in case of smaller and less busy bridges. Closing down or reducing traffic on crossings of greater importance for the construction period, however, can result in major delays and revenue loss for commerce and transportation as well as increasing the traffic load on alternate route bridges. Multiple-deck bridges may be the answer to this issue. A parallel deck can be built next to the existing one, without reducing the flow. Additionally, a new bridge can be designed as a twin or multi-deck structure. Several such structures have been built throughout the United States, among them:

- The New NY Bridge Project - the Tappan Zee Hudson River Crossing,
- SR-182 Columbia River Bridge,
- The Thaddeus Kosciusko Bridge (I-87), see Figure 1.1,
- The Allegheny River Bridge, Pennsylvania, which carries I76,
- Fred Hartman Bridge, TX, see Figure 1.2.

With a growing number of double deck bridges, additional, more detailed, studies on the interaction of such bridge pairs in windy conditions appears appropriate. Aerodynamic interference effects should be examined to assure the aerodynamic stability of both bridges. There are many studies on aerodynamic response of single deck bridges, but the literature on double-deck structures is not extensive. The experimental results from wind tunnels are still limited in number, as a parametric study is required, they can be very time consuming. Literature review shows that some investigation of the effects of gap-width and angle of wind incidence has been done [1], [2]. Most of the CFD computational studies that have been done were limited to 2D simulations [3], [4]. Therefore, it is desirable to investigate twin decks of various cross-sections, gap-to-width ratios, wind speed and direction using three-dimensional CFD simulations. After verification with wind tunnel test results, this type of analysis could become a powerful tool for future designs as well as for monitoring of existing bridges.



Figure 1.1: Thaddeus Kosciusko Bridge, NY, by Njhepler at English Wikipedia, CC BY 2.5,
<https://commons.wikimedia.org/w/index.php?curid=12452015>



Figure 1.2: Fred Hartman Bridge, TX, by United States Coast Guard, PA2 James Dillard - U.S. Coast Guard Visual Information Gallery U.S. Coast Guard Visual Information Gallery Home, Public Domain, <https://commons.wikimedia.org/w/index.php?curid=3499375>

1.2. Proposed analysis methods

This study was performed on a generic cross-section segment of a bridge deck model in an unsteady air flow. The analysis methods cover preliminary simulations, such as selection between Reynolds Averaged Navier-Stokes (RANS) equations with different turbulence models versus large eddy simulations (LES), and a mesh density study. The main purpose of the research is to: characterize static and dynamic responses of the decks with computation of steady state aerodynamic forces and pitching moment in RANS simulations as well as computations of the time history of aerodynamic forces and pitching moment obtained from LES simulations, and moreover, to characterize the upstream deck wake with respect to the downstream deck. Static simulations include a parametric study with various angles of wind incidence, different wind speed values and a study of gap-to-width ratios.

2. CFD model

2.1. General information

The CFD model is a representation of wind tunnel experiments. The domain geometry consists of three parts: the WT nozzle, trapezoidal transition part, and the main cube modeling the room. The dimensions are such that the boundary conditions don't have a significant influence on the flow around the decks. The model is long enough for the flow to be developed in front of the decks and there is no reverse flow at the pressure outlet. All outer surfaces of the model, excluding the inlet and outlet surfaces, have a no-slip wall boundary condition applied. The model is presented in Figure 2.1.

An initial test of bridge deck interaction with the incoming flow, a reference case is considered that does not have twin bridge decks. The model was created by removing the downwind deck from the domain. An example mesh around the decks is presented in Figure 2.2. The mesh is denser around the decks to capture in detail the interference between the decks.

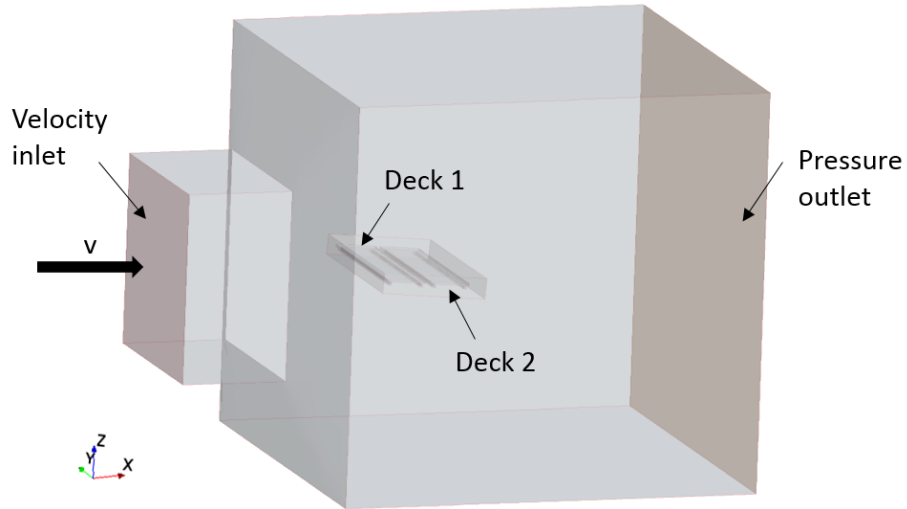


Figure 2.1: The computational domain

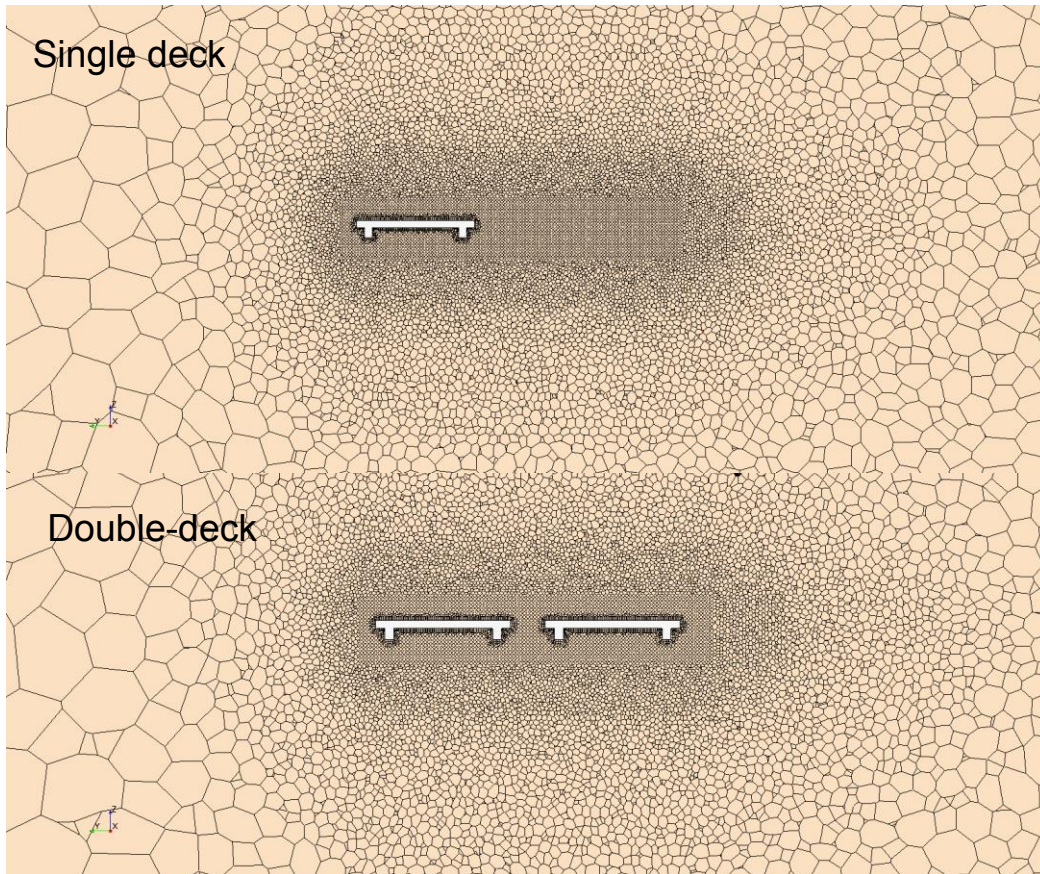


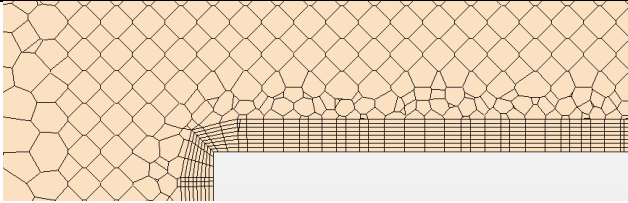
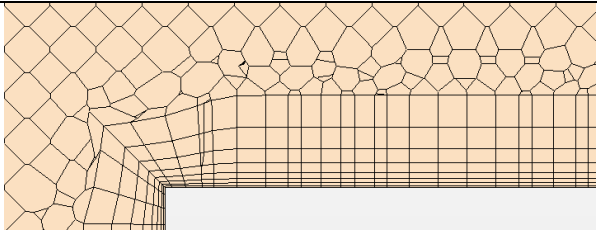
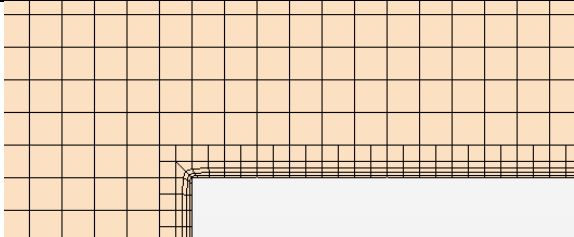
Figure 2.2: An example mesh around single and double deck cross sections

2.2. Mesh study

The influence of mesh density on the results is investigated in the first step of this study. In all cases a prism layer with constant thickness is created around the decks to provide layers of prism cells next to the wall. The ‘all Y+ treatment’ option is used, which uses a blended wall law to estimate shear stress if $5 < Y^+ < 30$. Two prism layer stretching values are considered. The first stretching value is 1.0, with 1, 2, 4, 8 and 16 layers (which gives $Y^+ = 40, 21, 9.4, 3.7$ and 2.1 accordingly). The second stretching value is 1.5, with 8 layers (which gives $Y^+ = 1.3$). The number of volume cells varies from approximately 3 to 4 million cells.

Two types of meshing techniques are taken into account. The polyhedral mesher is suited to complex, multi-region geometries. These cells usually have 12 to 14 faces. The trimmer mesher uses predominantly hexahedral mesh cells with trimmed cells next to surfaces. Table 1 shows which meshing techniques were used in the simulations with a detail view of the resulting prism layer around a corner of a deck.

Table 1: Types of meshes used in the simulations

Mesher	Prism layer stretching	Resulting mesh around the deck
Polyhedral	1	
	1.5	
Trimmer	1.5	

An unsteady RANS solver was used in the computations as well as Large Eddy Simulation model. The simulations were kept running until the flow reached a steady state and force and moment components on the stationary decks converged to a constant value.

Computations using the URANS solver with the k-eps turbulence model and polyhedral mesh were performed for different thicknesses of the first prism layer. Moreover, for the densest mesh (and thinnest first layer) LES computations were done with polyhedral and trimmer meshers. The resulting graphs are presented in Figure 2.3 and Figure 2.4. The parametric study shows that the biggest differences in drag and lift forces for both decks are between the lowest ($Y+=1$) and highest considered values of $Y+$ ($Y+=40$). Two highest values of $Y+$ give very close values for all components except for pitch moment on deck 1. For the instance of the lowest $Y+$, most simulations give very similar results except for LES with polyhedral mesh. Only the drag force and pitch moment acting on deck 1 don't depend on the solver used.

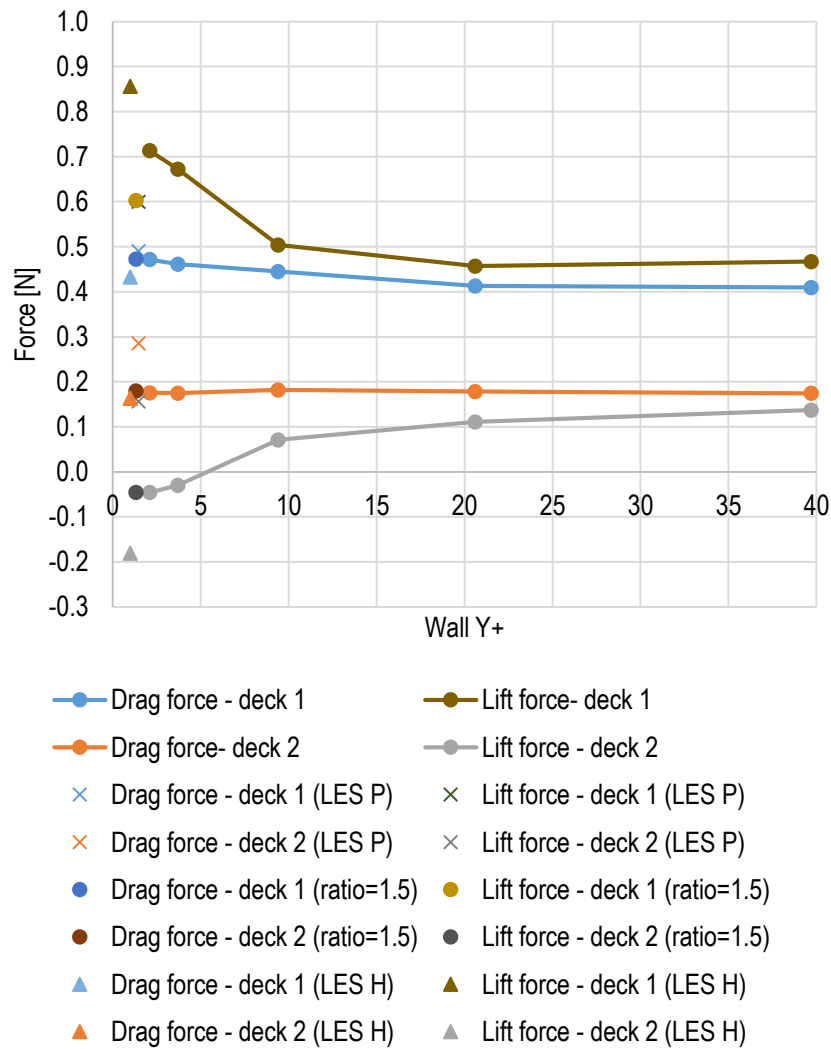


Figure 2.3: Force component values vs. wall Y+

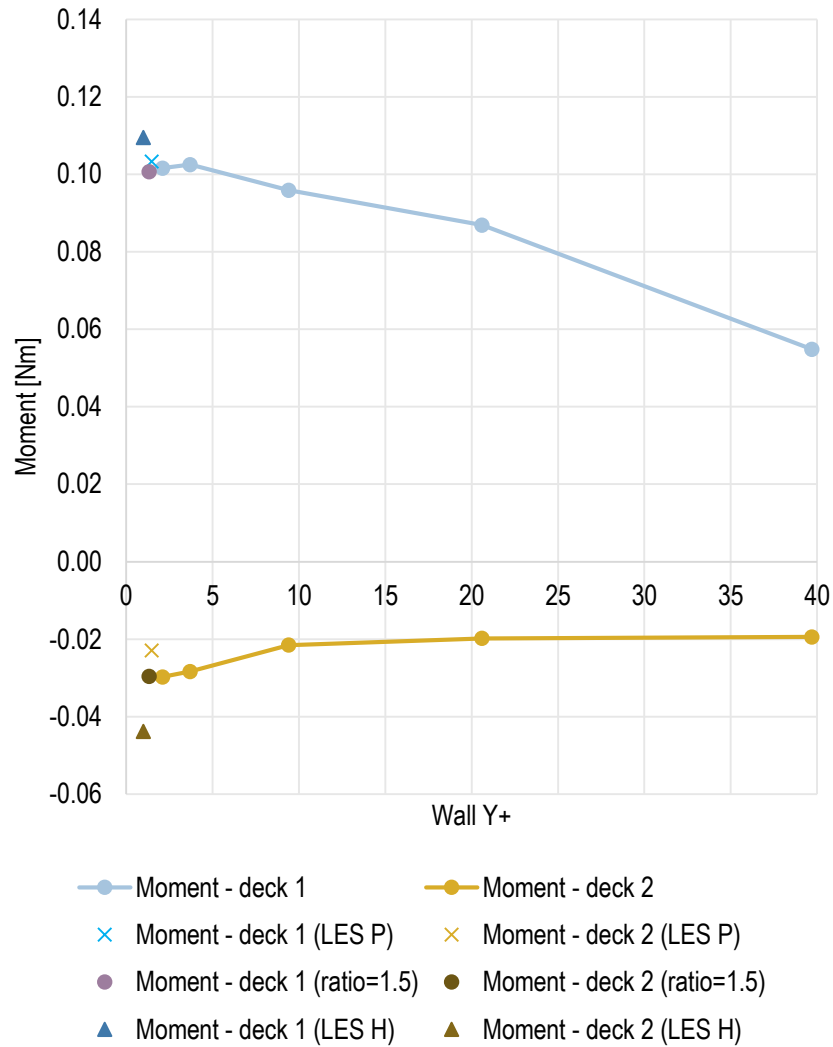


Figure 2.4: Moment component values vs. Y+

The influence of mesh type and mesh density on the force components are also shown in Figure 2.5 and Figure 2.6 in the form of column graphs. The first two columns refer to polyhedral and hexahedral mesh with $Y+=20$, the next two columns refer to polyhedral and hexahedral mesh with $Y+=1$, and the last column – to LES simulations.

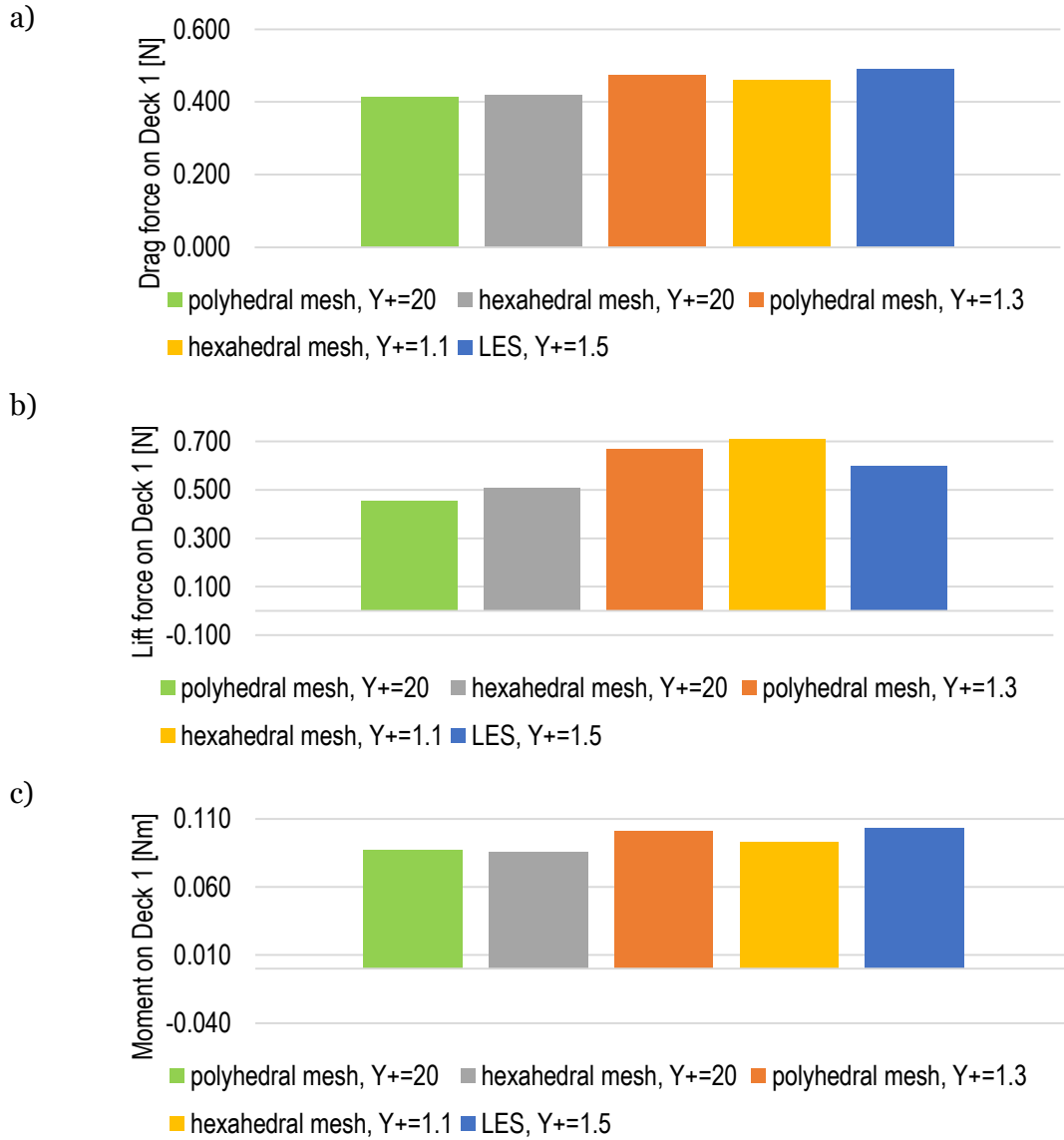
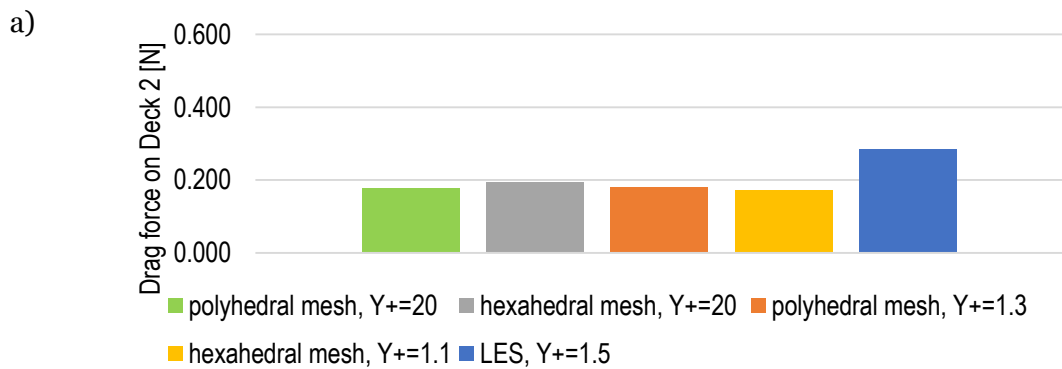


Figure 2.5: Mesh influence on force and moment components values acting on deck 1



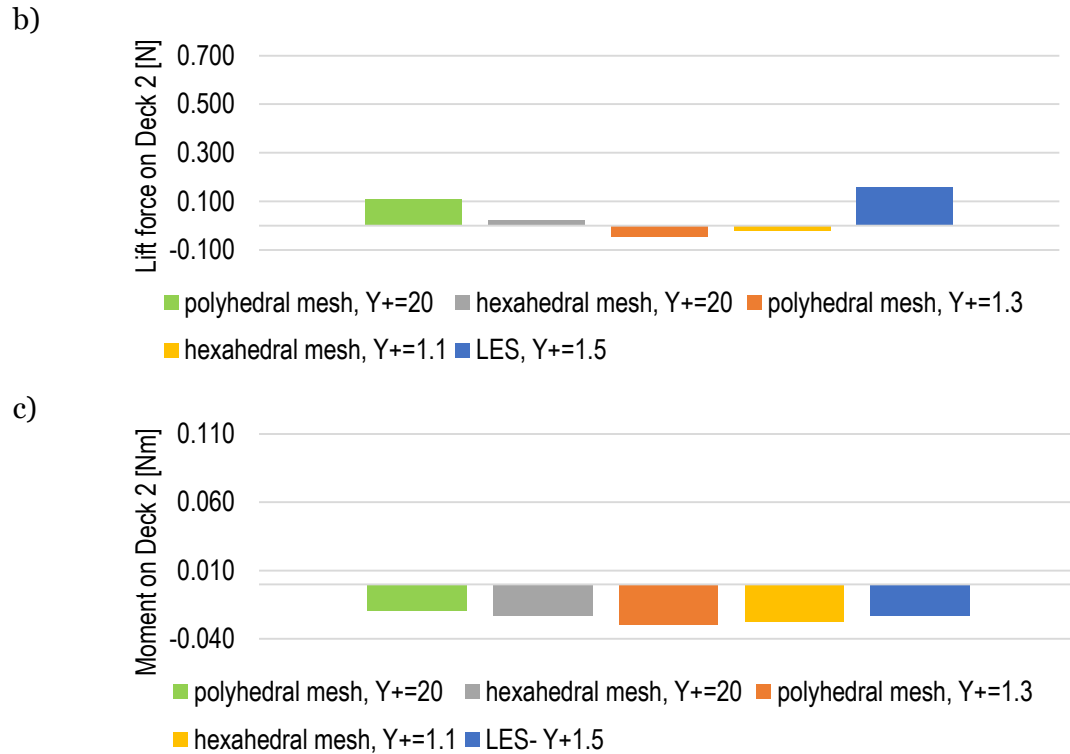
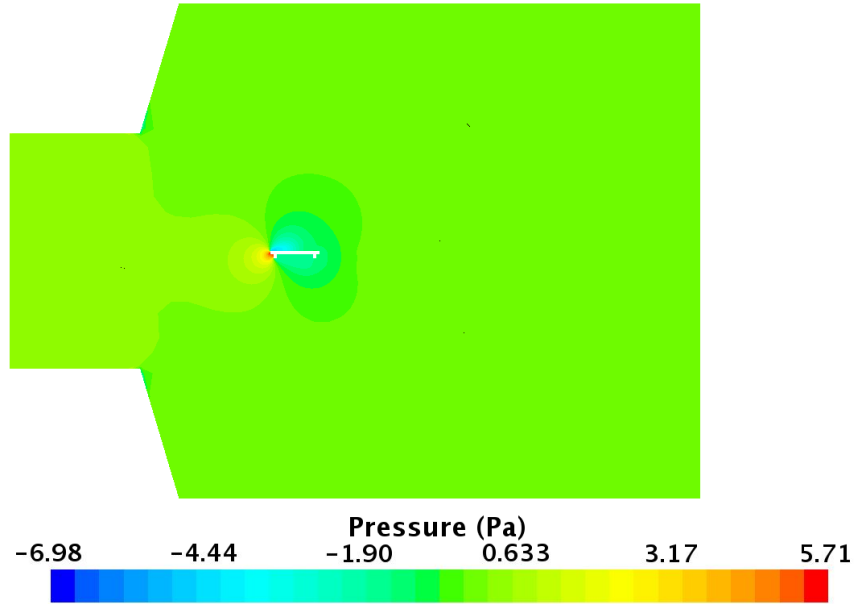


Figure 2.6: Mesh influence on force and moment components values acting on deck 2

2.3. Pressure and velocity fields with a single deck

The pressure and velocity contour plots for a single deck in a wind tunnel are depicted in Figure 2.7 and Figure 2.8. The general view shows that the flow in the domain reached a steady state. The zoomed-in views of the deck surroundings allow investigation of these fields in greater detail. Pressure reaches the highest values on the upwind side – vertical and bottom surfaces. The lowest (negative in value) pressure is located on the top surface, right at the front. Moreover, multiple separation points can be seen in the velocity contour plot as the cross-section is not streamlined.

a)



b)

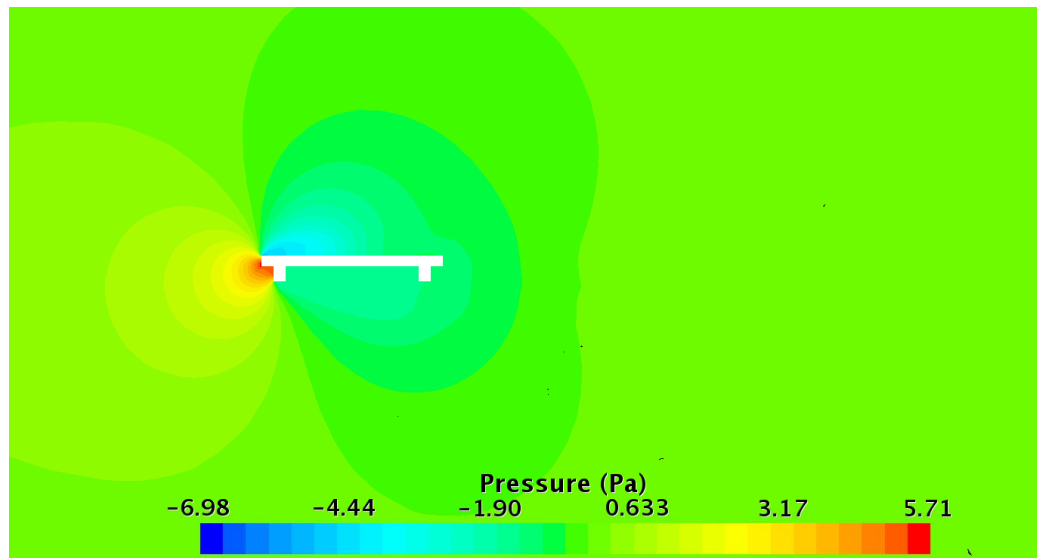
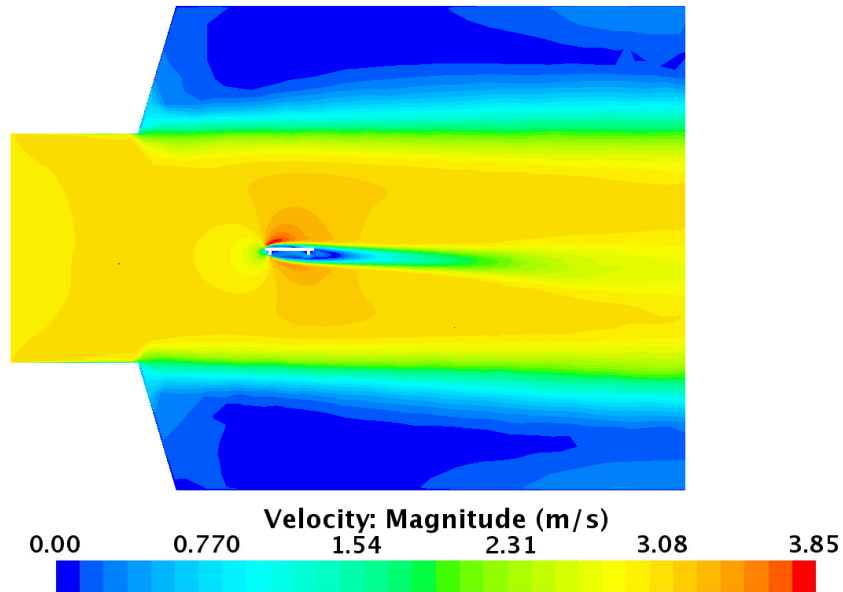


Figure 2.7: Single deck. Pressure plot on the mid surface of the domain a) general view, b) the area around the deck

a)



b)

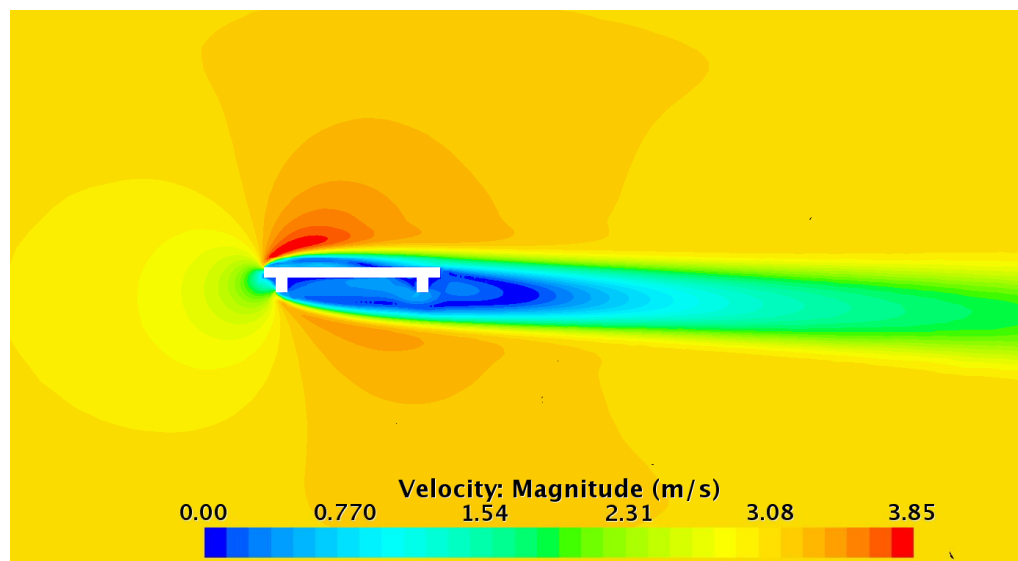
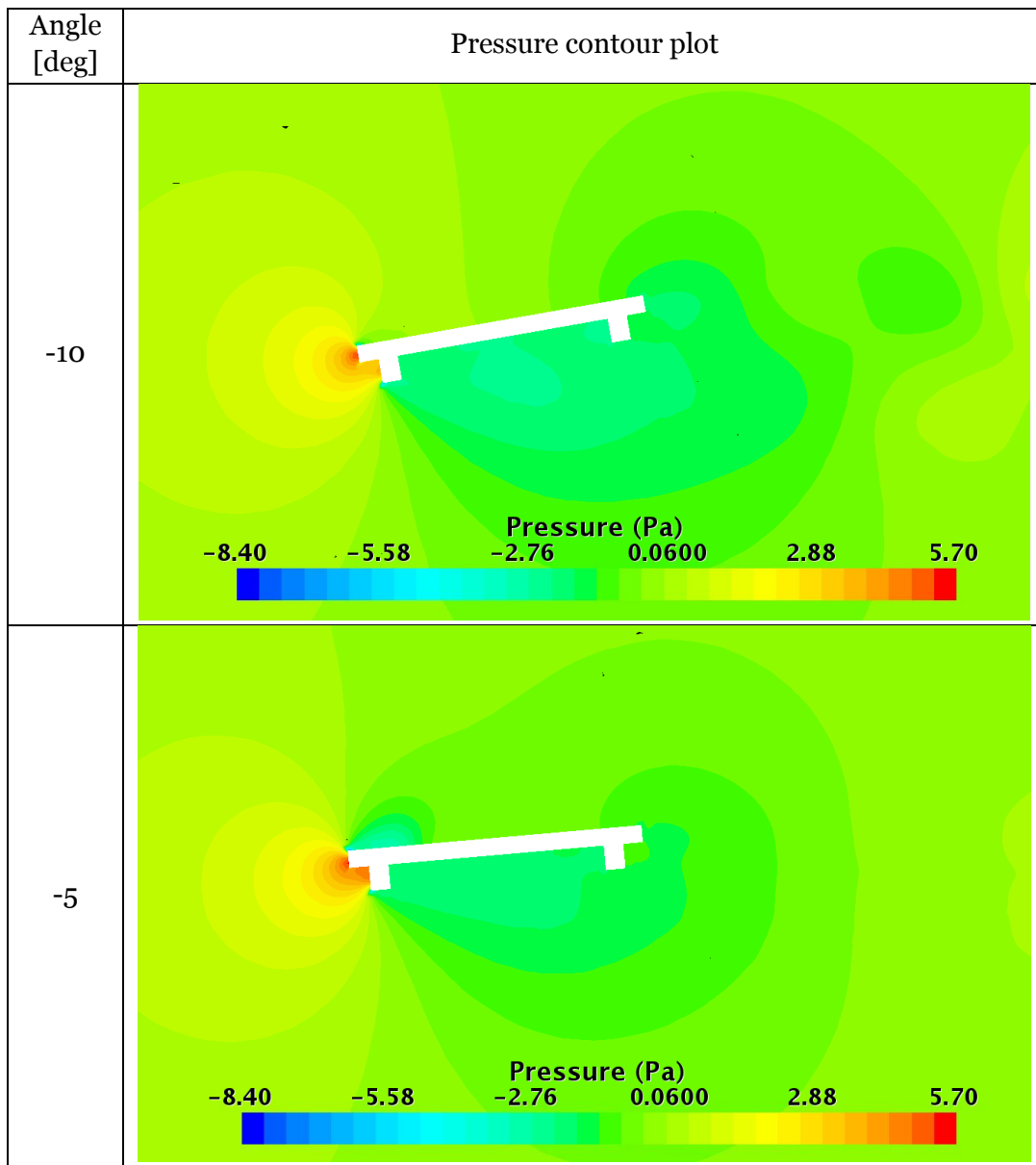


Figure 2.8: Single deck. Horizontal velocity plot on the mid surface of the domain a) general view, b) the area around the deck

Pressure distribution around the deck was checked for different flow directions. Angles in the range of -10 deg to 10 deg with a 5 deg intervals were selected. The resultant pressure fields on a section through the deck are collected in Table 2. Table 3 summarizes velocity field contour plots. The extreme values of pressure and velocity can be found in Table 4. The minimum pressure applied to the deck, equal -8.37 Pa, is located at the top upwind corner of the deck and occurs when the angle equals 5 deg. The highest positive value 5.7 Pa, in the parallel flow, is applied to the upwind surface of the deck. The velocity field on the central plane changes with the angle of attack. It is smooth in the -5 deg to 5 deg range. For the angles -10 deg and 10 deg a more turbulent flow is formed behind the deck.

Table 2: Pressure field contour plots for a single deck bridge at varying angle of attack



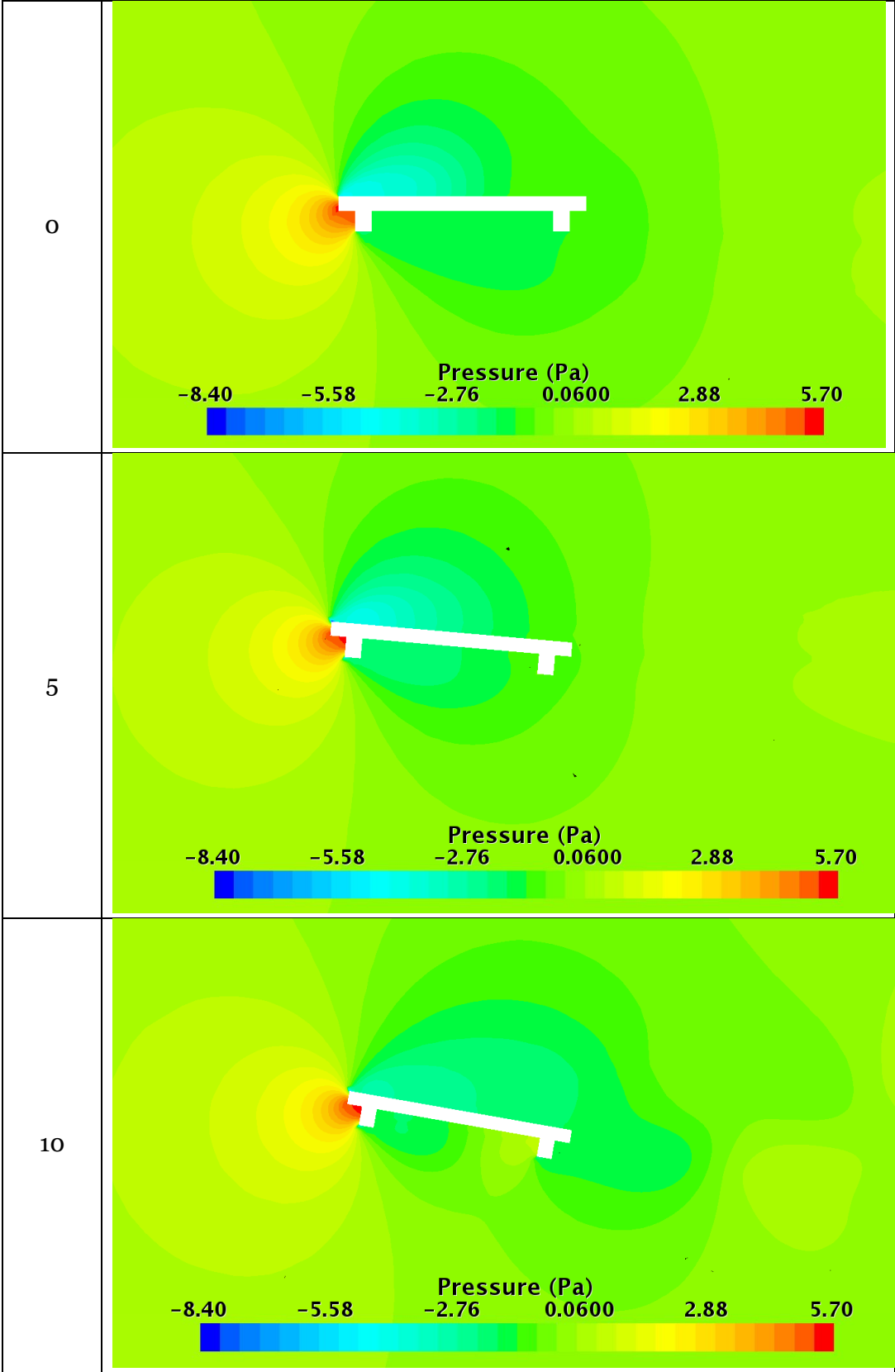
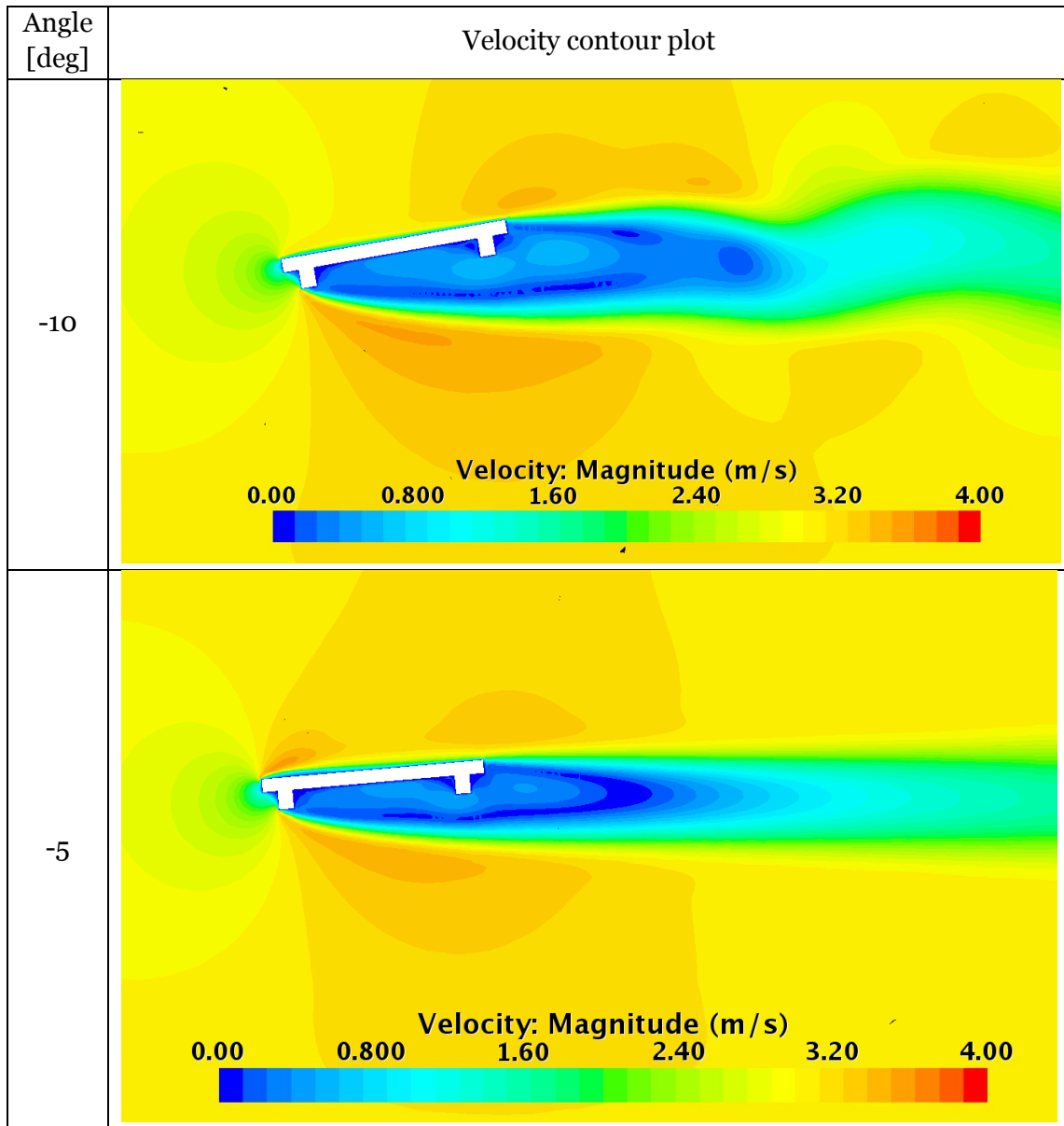


Table 3: Velocity field contour plots for a single deck bridge at varying angle of attack



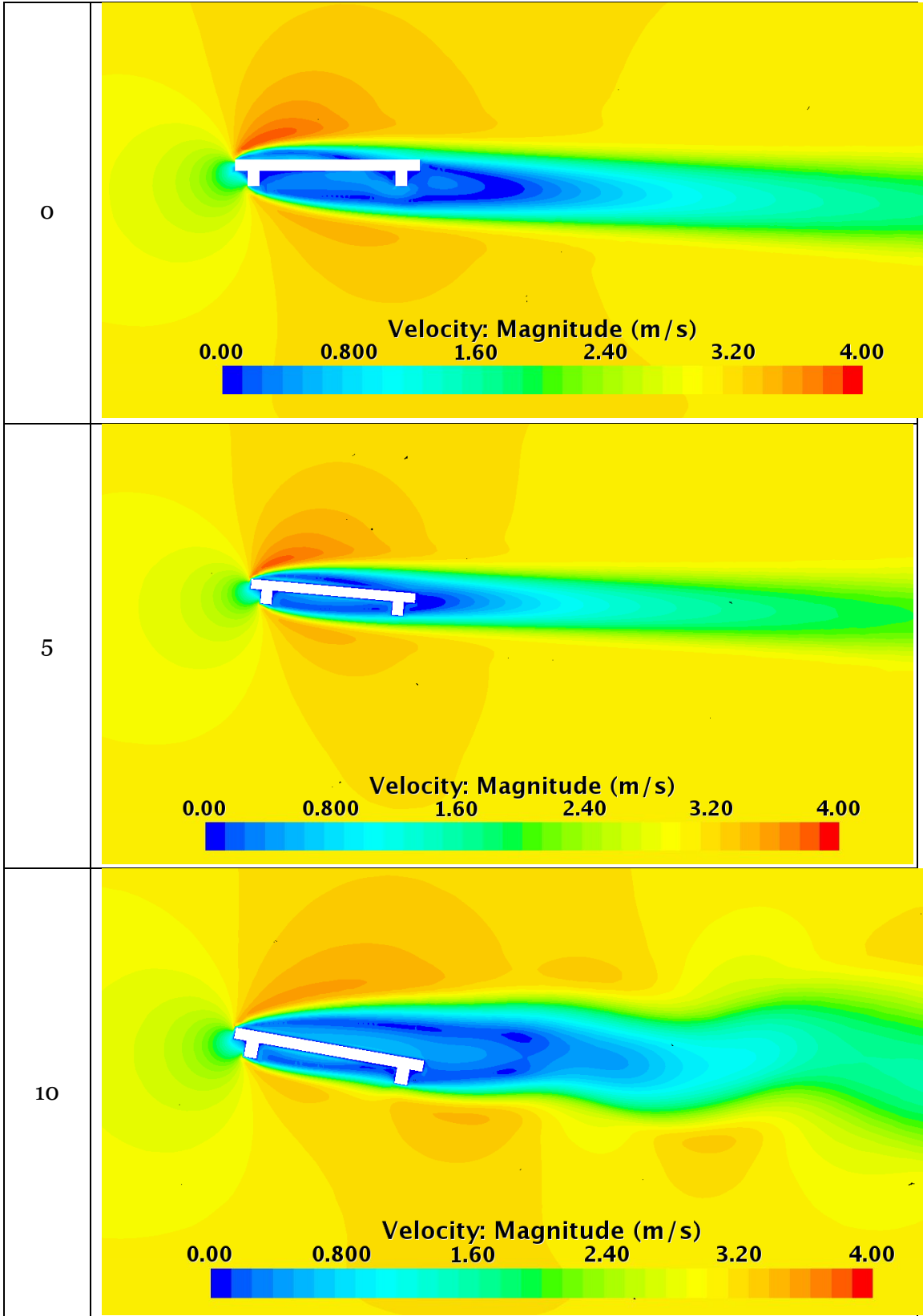


Table 4: Extreme values of pressure and velocity for a single deck

Angle [deg]	Pressure [Pa]		Velocity [m/s]
	min	max	max
-10	-6.76	5.37	3.54
-5	-7.51	5.48	3.58
0	-6.98	5.70	3.85
5	-8.37	5.34	3.86
10	-6.23	5.38	3.98

3. Analysis of double deck bridges

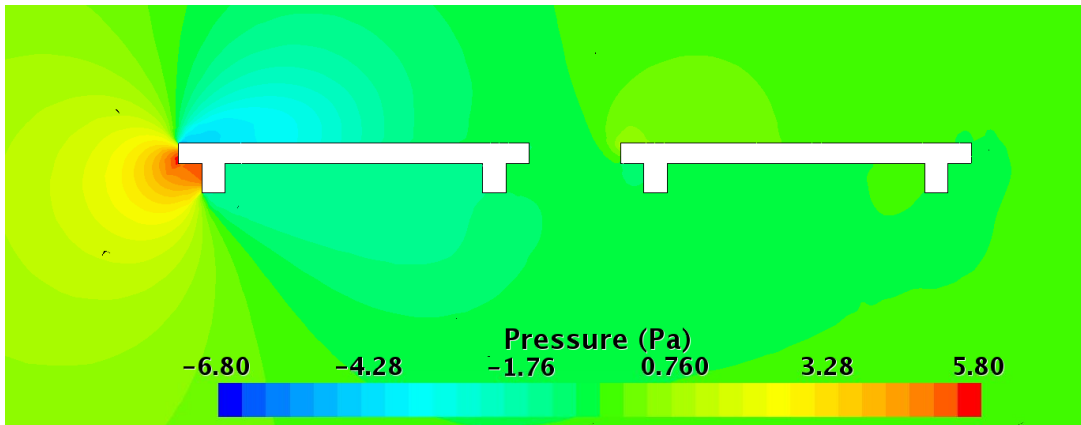
3.1. Pressure and velocity fields on double decks

Figure 3.1 illustrates pressure contour plots around double deck cross-sections with a 0.1 m gap. The figures show a comparison of pressure and velocity fields for two models: URANS solver and LES with a low Y^+ . A polyhedral mesh was used in all cases. The value ranges are kept constant for an easier comparison.

The differences are not significant in the case of the upwind deck, with the pressure values very similar in both instances. The flow field in a LES simulation changes in time and here only one image was shown. The discrepancies are higher for the downwind deck. It stays in the wake of the upwind deck and small differences in the field around it influence the downwind deck. It is best seen for the LES simulation where the vortices form behind the first deck. The URANS computations give an averaged solution.

A more detailed description of pressure field around the decks is depicted in Figure 3.2 to Figure 3.9. Sets of points were chosen on each surface of the model, where pressure values were recorded. Results for LES computations are time-averaged. The results obtained with the $k-\epsilon$ model are very similar, regardless the mesh size at most of the points, except for the ones located in the corners. Figure 3.2 b) shows that the values are two times higher for $Y^+=20.6$. As the pressure gradients are high in these regions it is important to use a denser mesh, so that no information is lost. A comparison of two models with the same Y^+ shows that they give similar results in the areas of less turbulent flow, like the front of the deck 1 or the upwind part of the top surfaces. The downwind regions experience the influence of eddies.

a)



b)

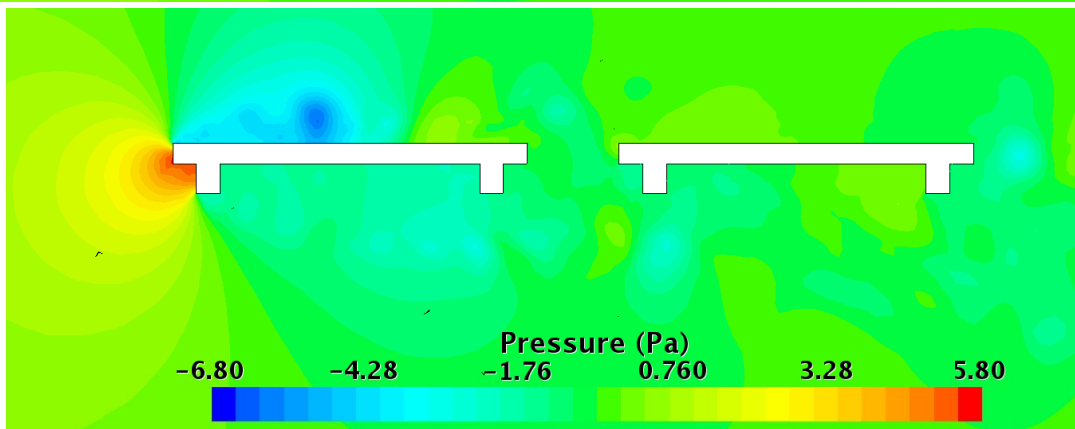


Figure 3.1: Pressure contour plot around the decks, a) URANS, b) LES, polyhedral mesh, $Y^+=1$

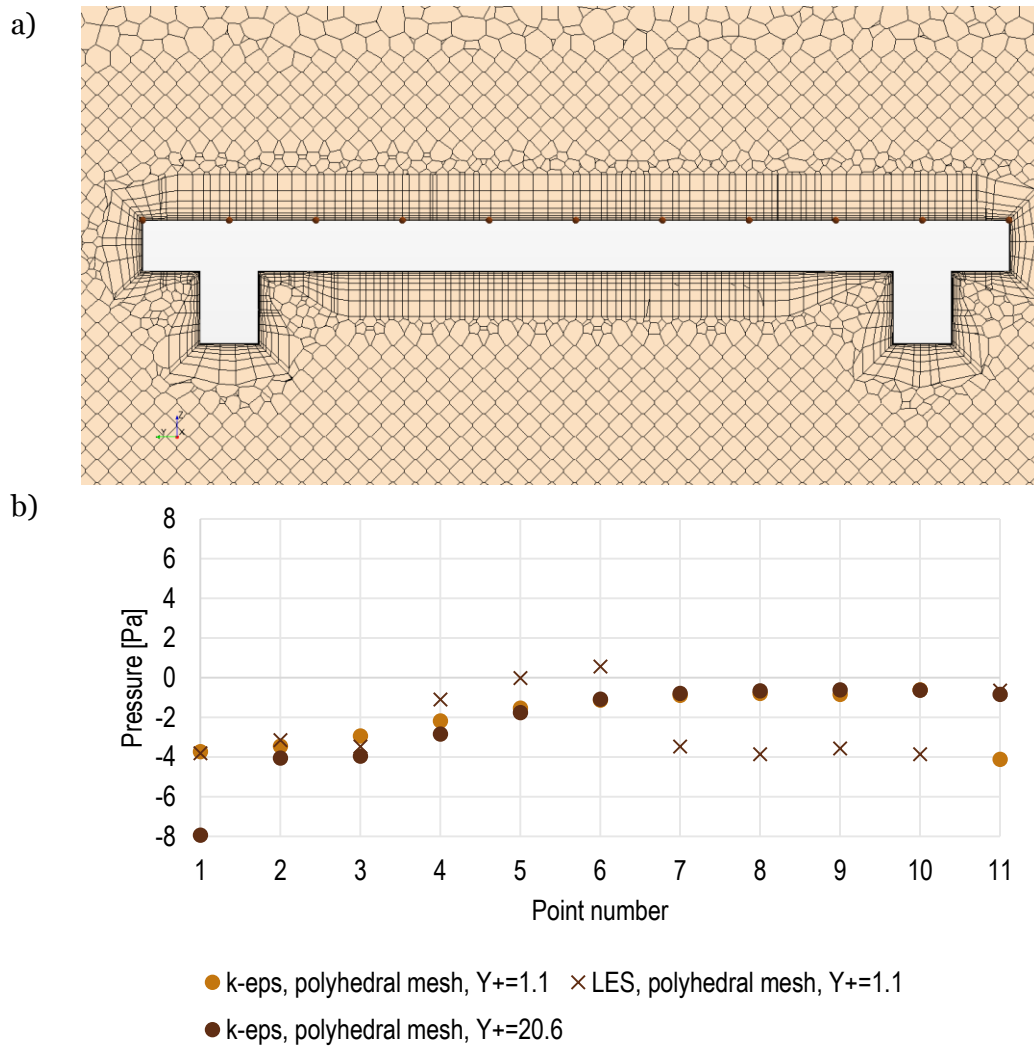


Figure 3.2: Pressure on the symmetry line of the top surface of deck 1, a) location of measured points, b) pressure values

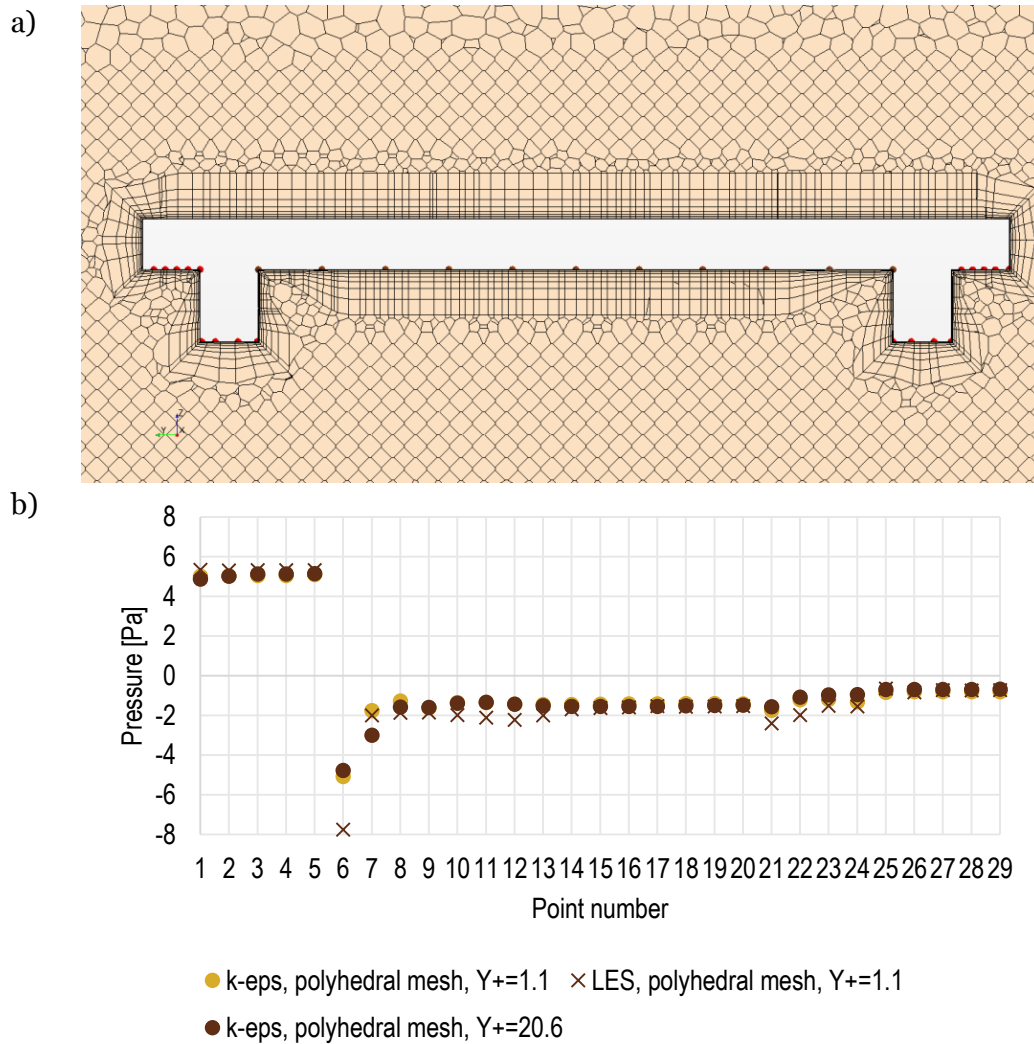


Figure 3.3: Pressure on the symmetry line of the bottom surface of deck 1, a) location of measured points, b) pressure values

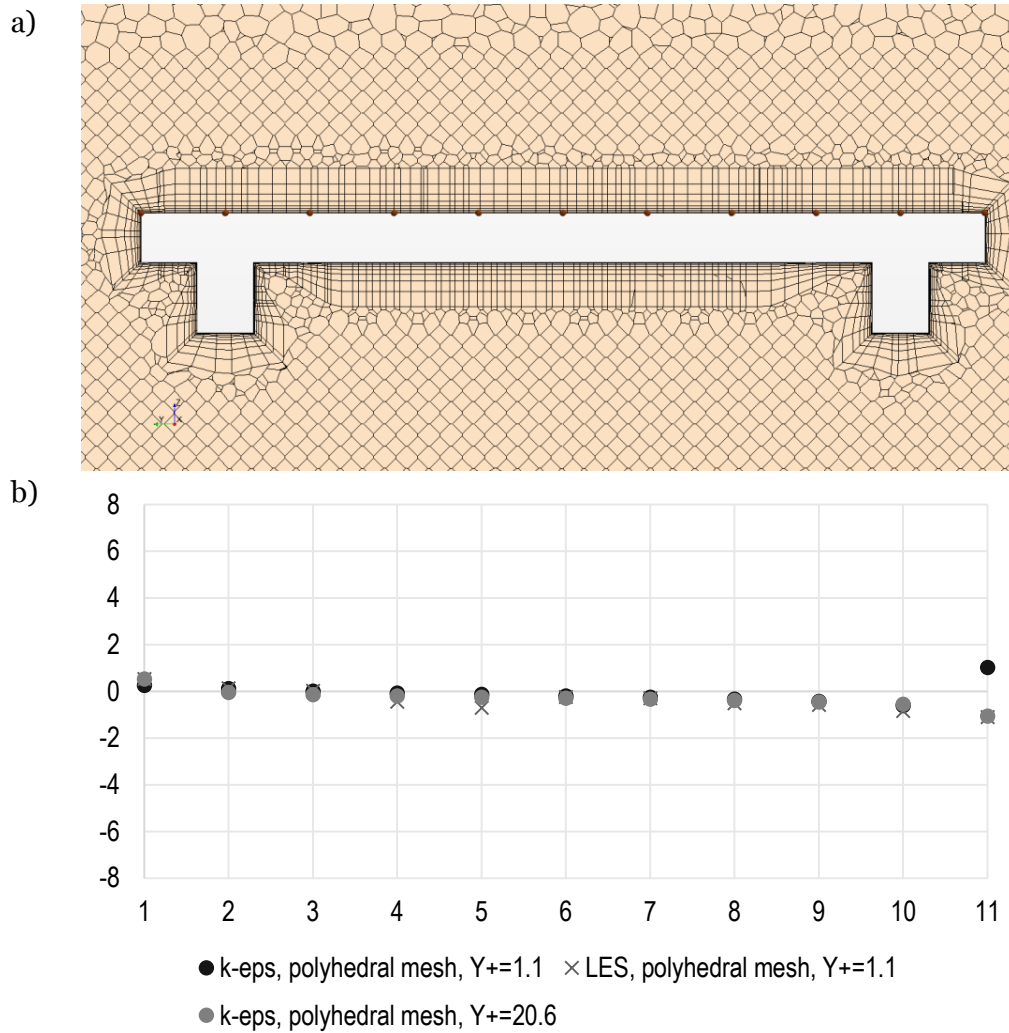


Figure 3.4: Pressure on the symmetry line of the top surface of deck 2, a) location of measured points, b) pressure values

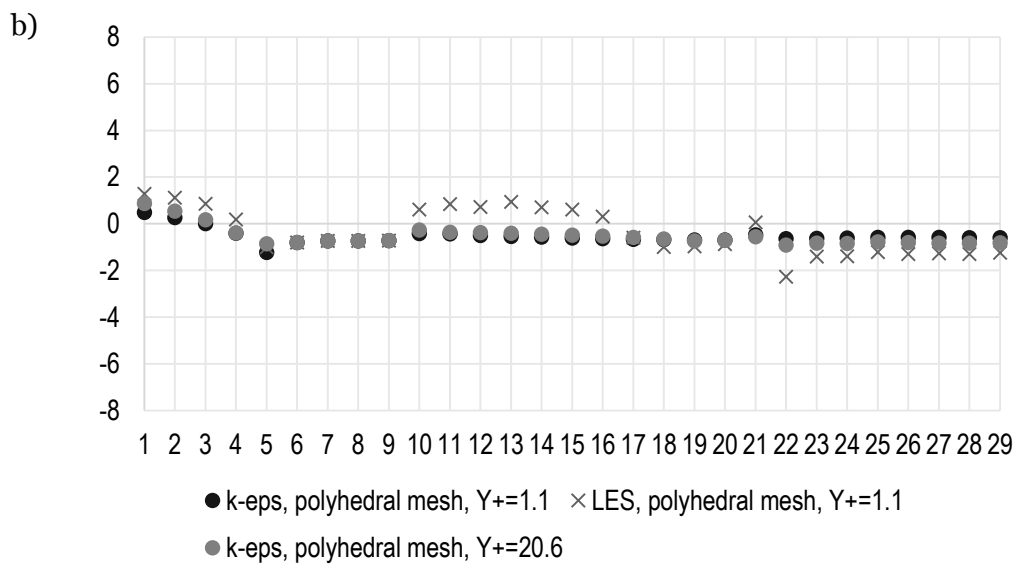
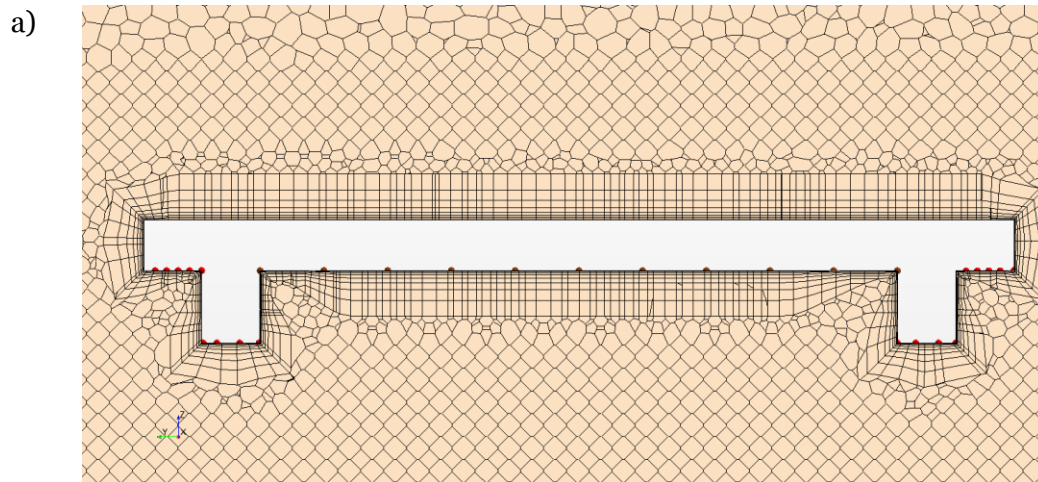


Figure 3.5: Pressure on the symmetry line of the bottom surface of deck 2, a) location of measured points, b) pressure values

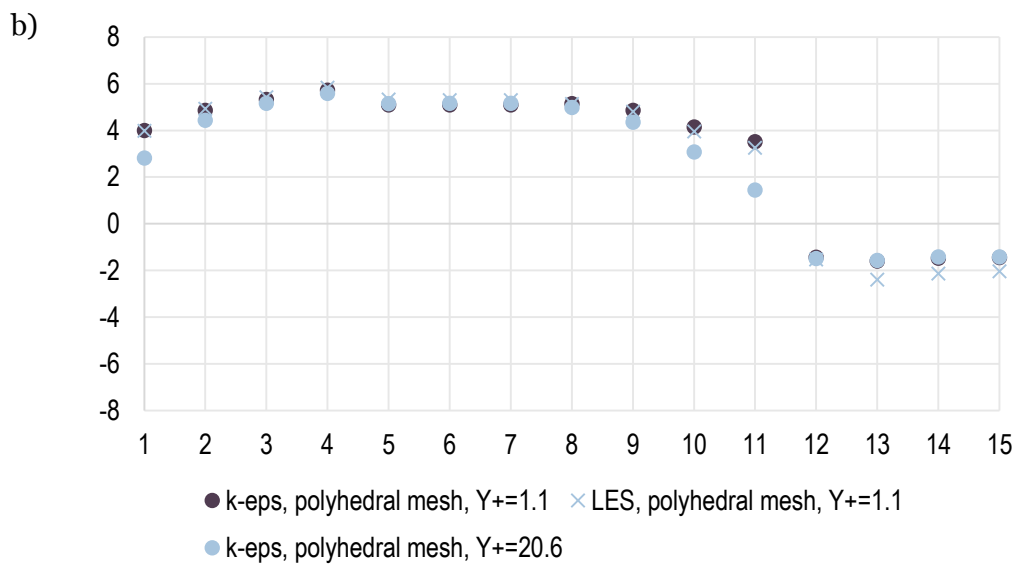
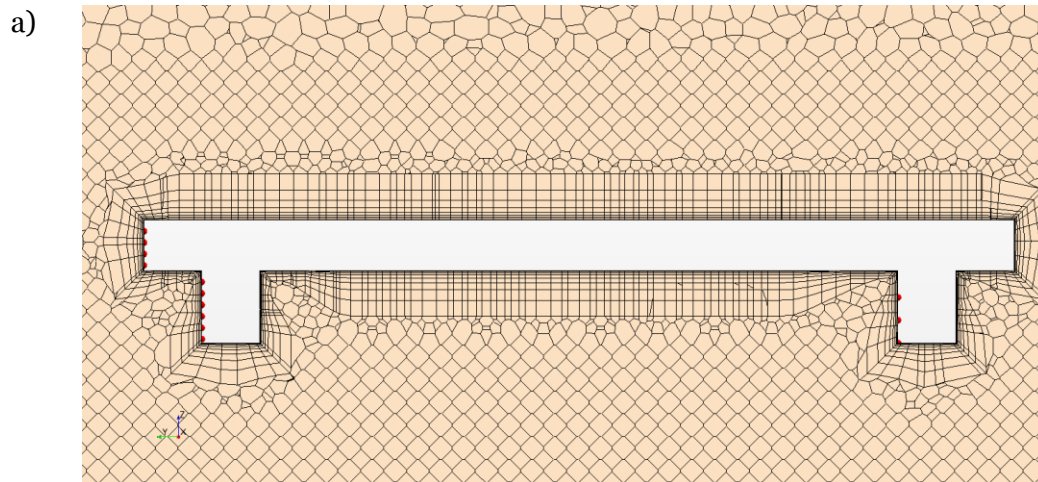


Figure 3.6: Pressure on the symmetry line of the upwind surface of deck 1, a) location of measured points, b) pressure values

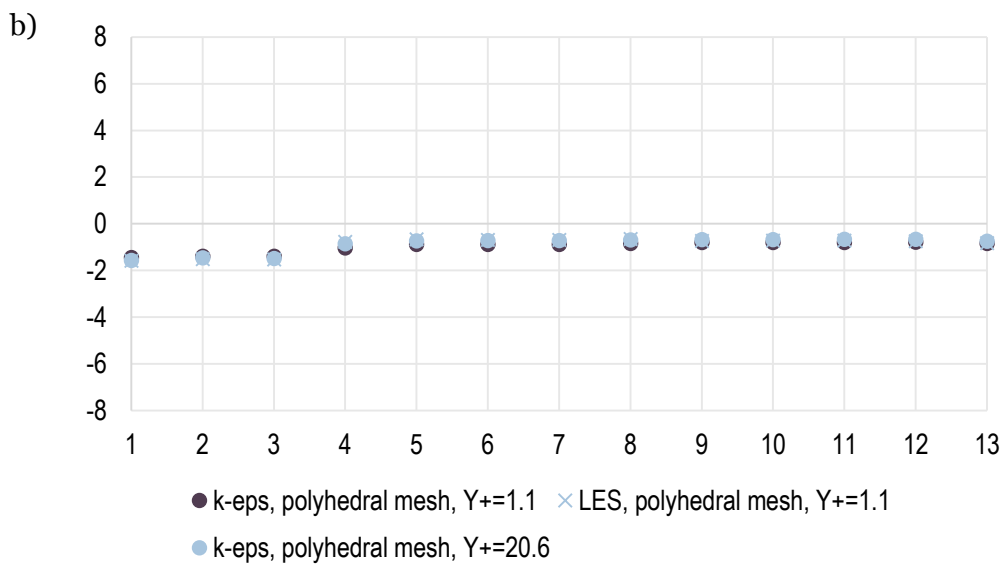
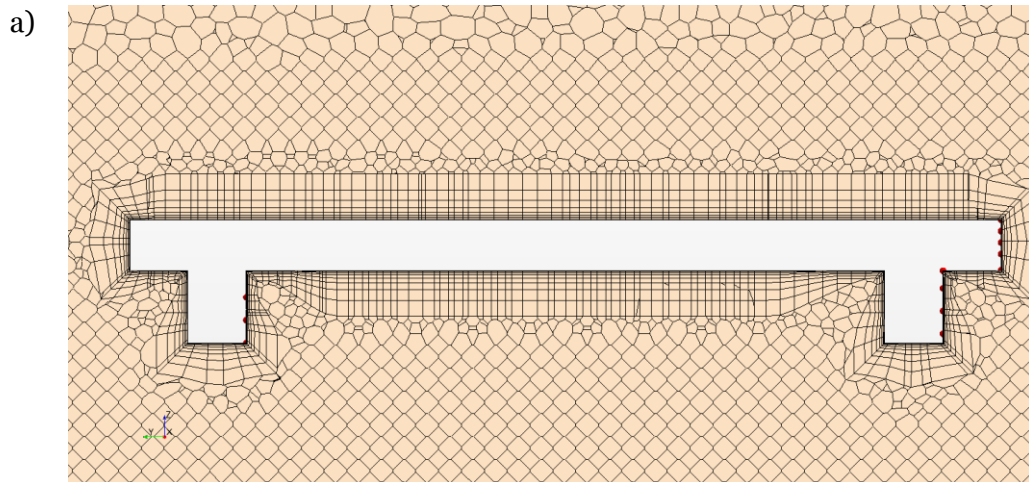


Figure 3.7: Pressure on the symmetry line of the downwind surface of deck 1, a) location of measured points, b) pressure values

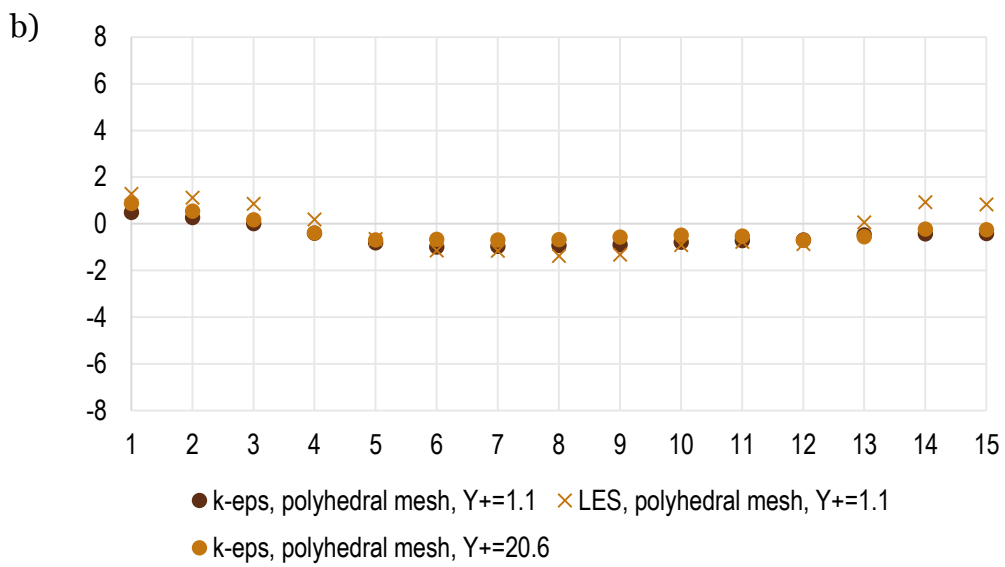
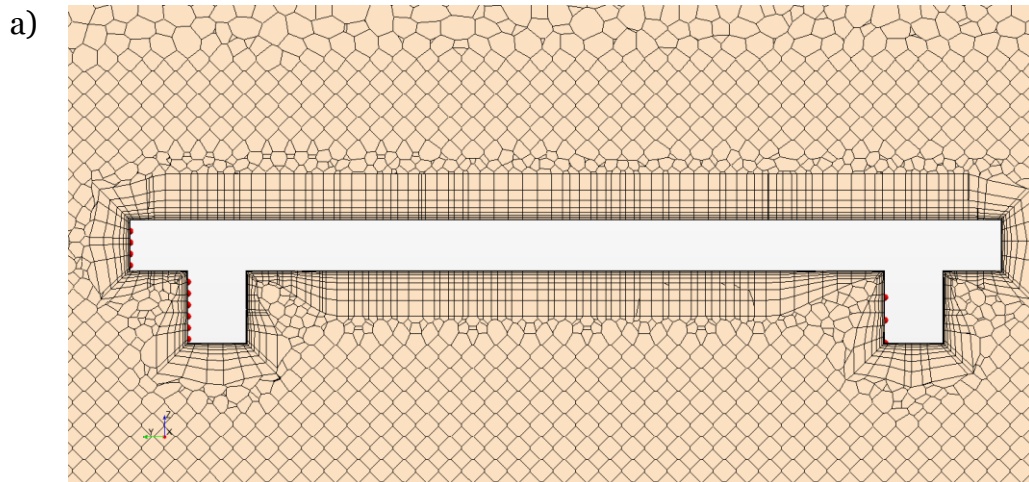


Figure 3.8: Pressure on the symmetry line of the upwind surface of deck 2, a) location of measured points, b) pressure values

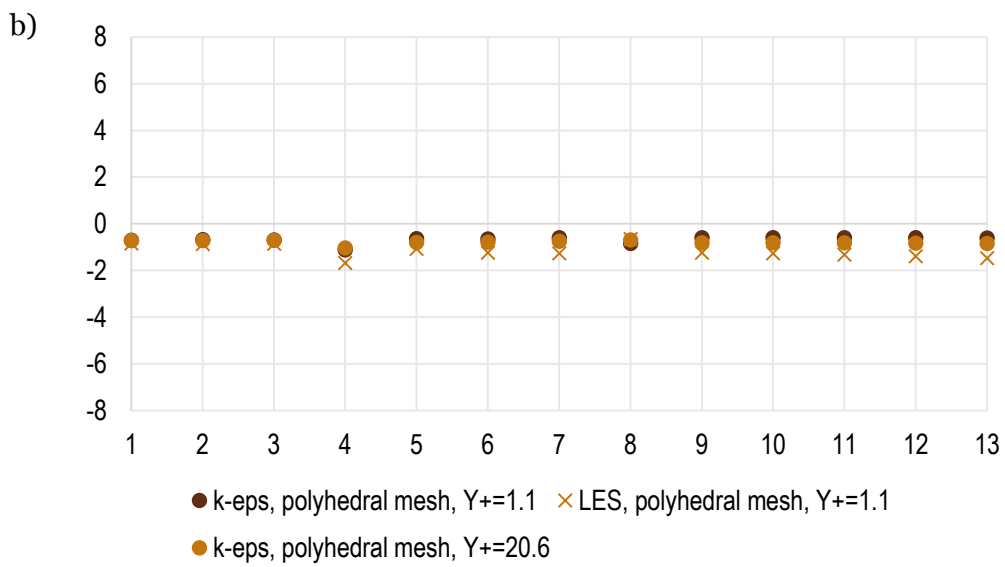
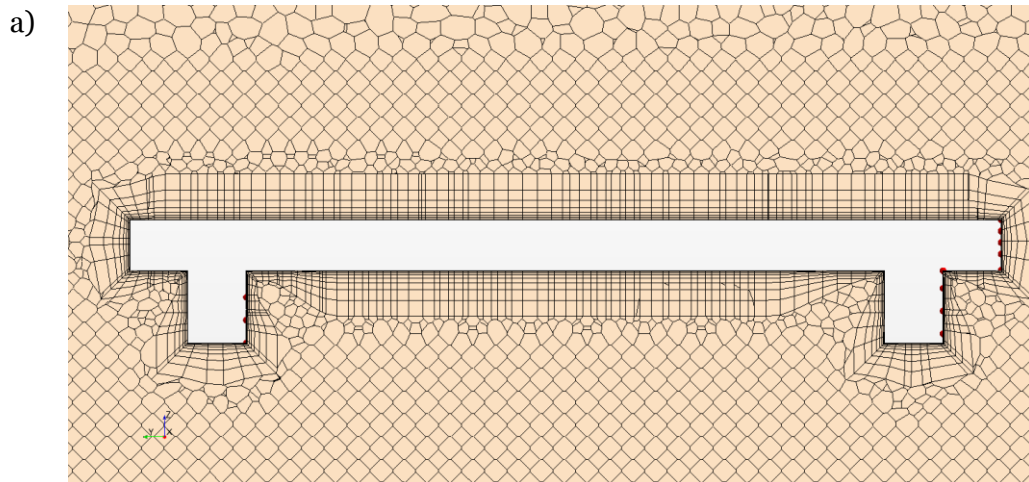


Figure 3.9: Pressure on the symmetry line of the downwind surface of deck 2, a) location of measured points, b) pressure values

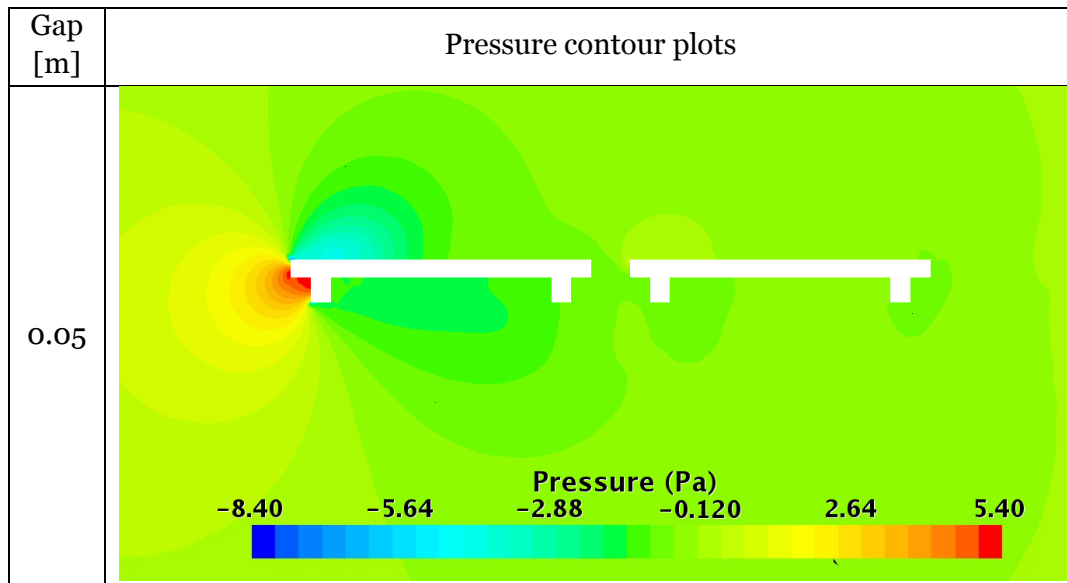
3.2. Varying horizontal gap between decks

The influence of the horizontal distance between two decks on pressure and velocity fields around them was investigated. The considered set of gaps is the following: 0.05, 0.1, 0.2, 0.3 m. Table 5 summarizes maximum and minimum pressure and velocity values acting on the upwind deck with different spacing between decks. The differences in values are very small. The biggest applies to the minimum pressure and equals less than 4%. Table 6 shows field plots of pressure and velocity depending on the deck spacing.

Table 5: Extreme values of pressure and velocity for a double deck with varying gap

Gap [m]	Pressure [Pa]		Velocity [m/s]
	min	max	max
0.05	-8.37	5.38	3.81
0.1	-8.38	5.40	3.80
0.2	-8.36	5.4	3.8
0.3	-8.39	5.40	3.81

Table 6: Pressure and velocity fields around double deck with varying gap



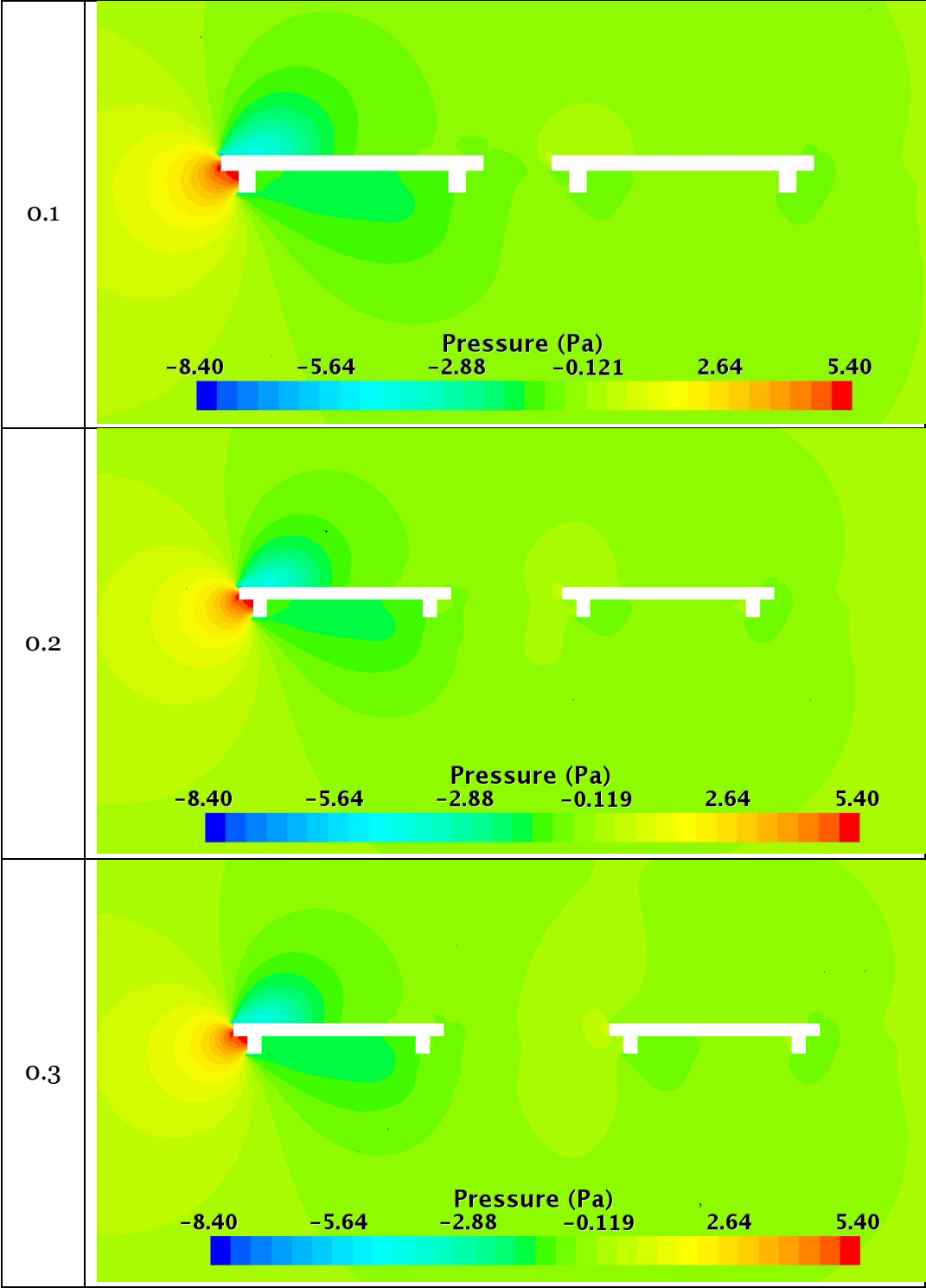
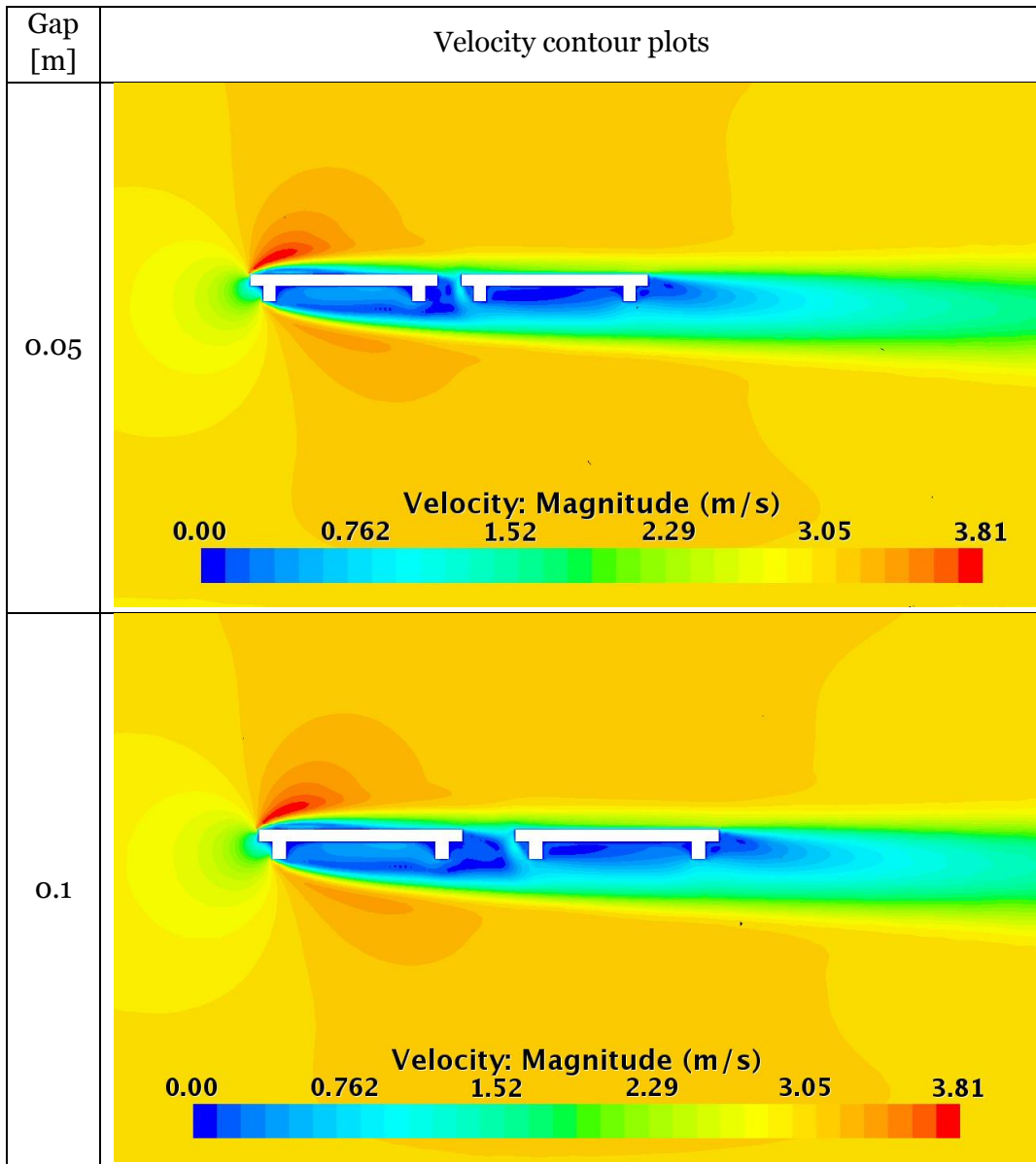
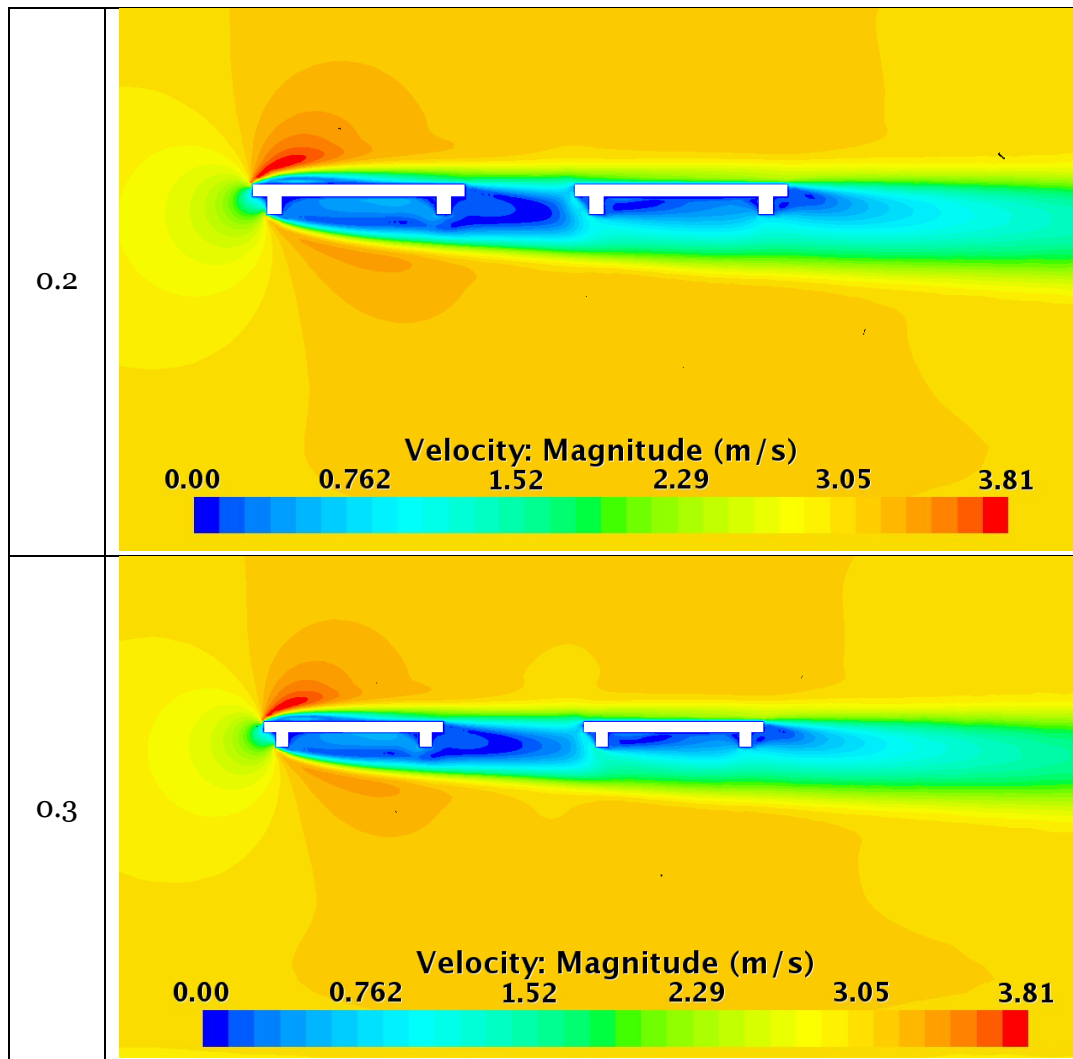


Table 7: Velocity field contour plots for a single deck bridge at varying gap





The combined results for drag, lift, and pitch moment acting on a single deck and a double deck can be seen in Figure 3.10 **Error! Reference source not found.**, Figure 3.11, and Figure 3.12. A comparison of force components on deck 1 and the single deck model show that there is only a slight difference in values. The deck spacing doesn't have a big influence on the forces acting on deck 1, they have almost constant values of 0.41 N. The drag is lower in magnitude on the downstream deck, because it is located in the upstream deck wake and it is shielded to some extent by it. This effect diminishes as the gap increases. A change of spacing from 0.05 m to 0.3 m causes the drag force to increase from 0.15 N to 0.25 N. In contrast, lift and moment don't vary significantly. The values for the upstream deck are by 15-20% higher than for a single deck and they are almost constant (varying between 0.45 N and 0.48 N) regardless the gap. The lift force on the downstream deck increases as the gap gets bigger, from 0.11 N for the smallest gap to 0.135 N for 0.2 m gap.

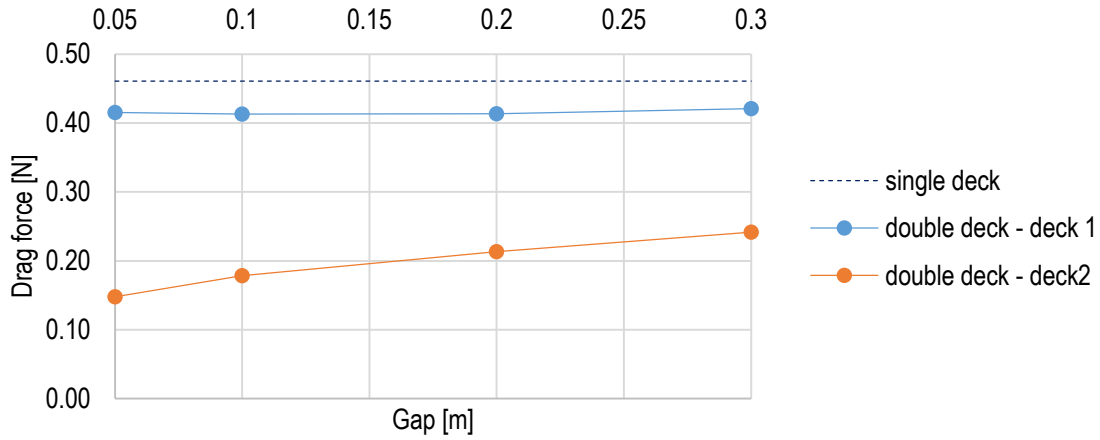


Figure 3.10: Gap influence on the drag force at parallel flow

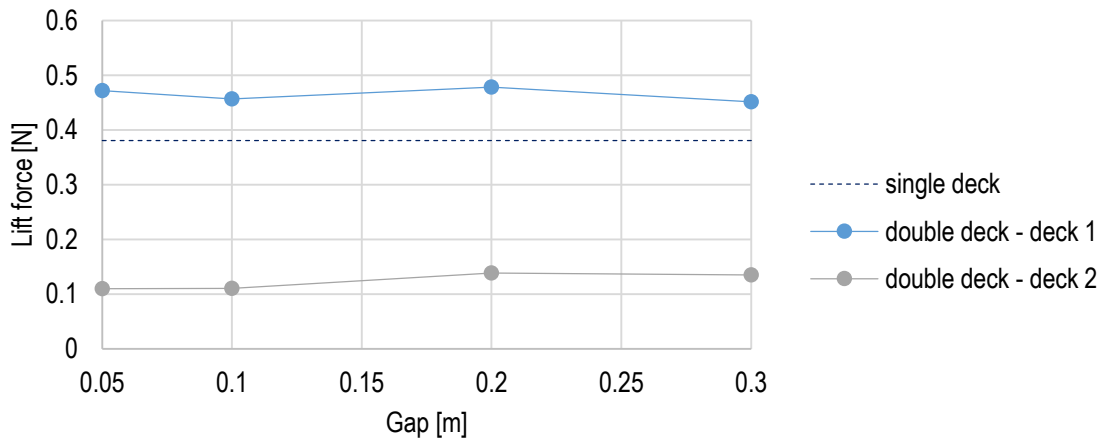


Figure 3.11: Gap influence on the lift force at parallel flow

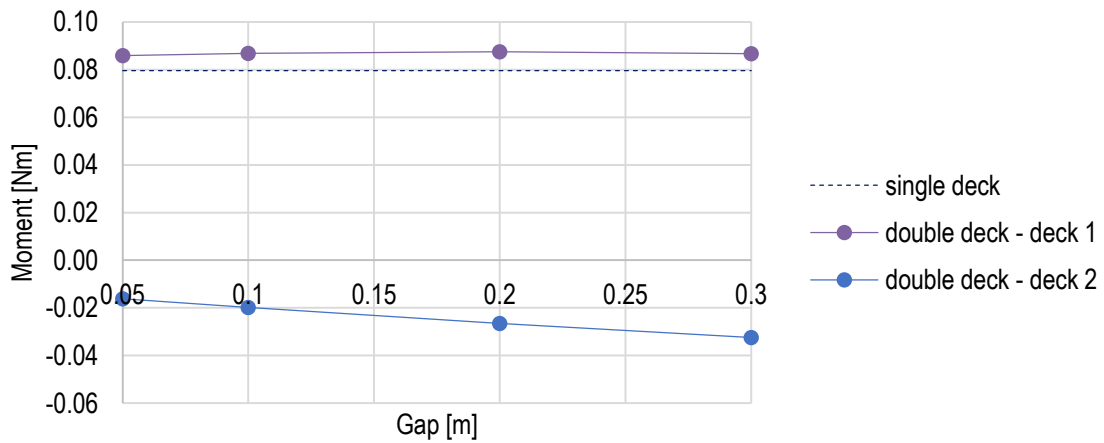
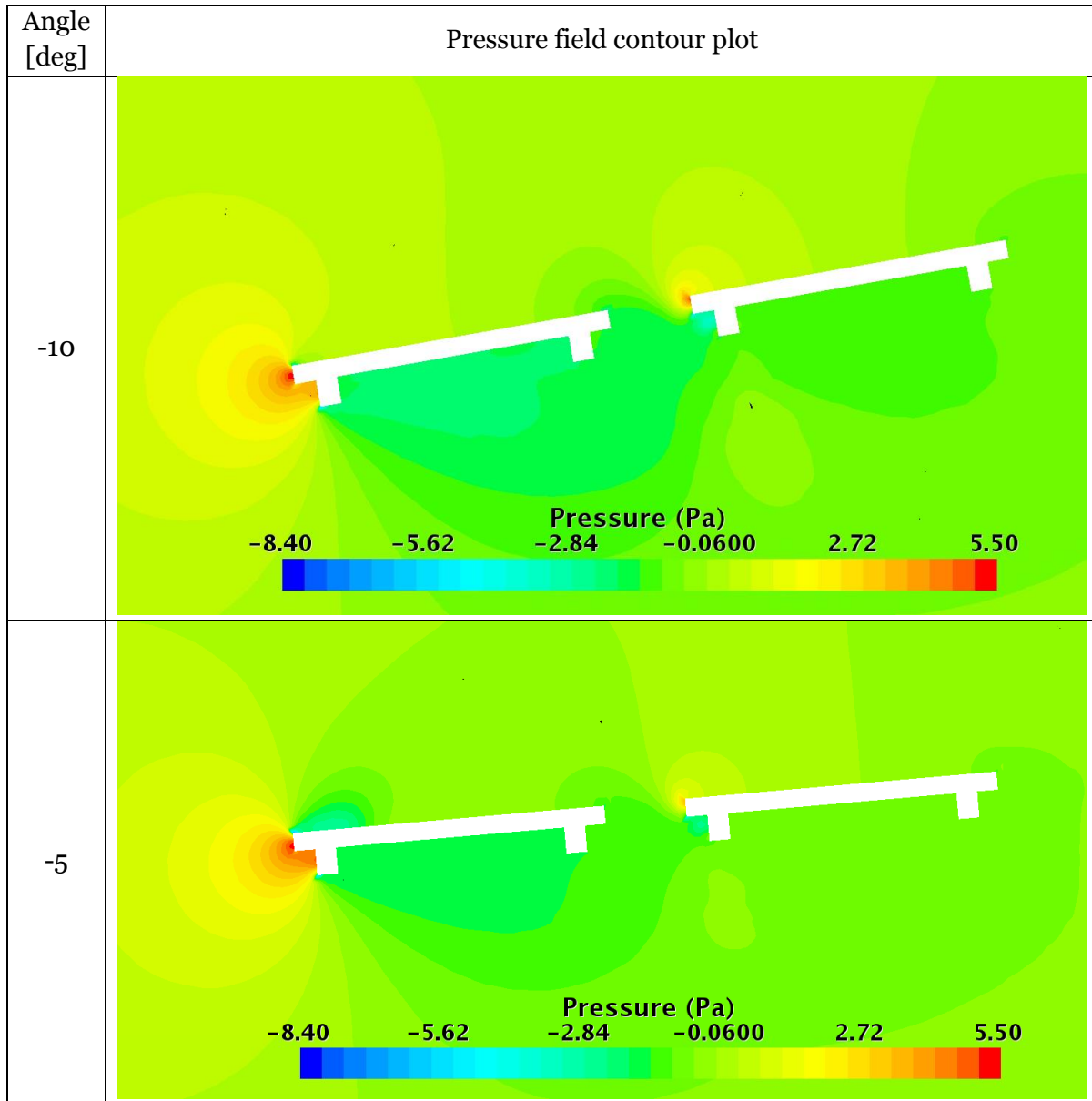


Figure 3.12: Gap influence on the pitch moment at parallel flow

3.3. Varying angle of attack

A set of five angles of attack were tested, which range from -10 degrees to 10 degrees in 5 degree increments. Pressure contour plots for double deck model with a 0.1 m gap are collected in Table 8 and velocity contour plots for the same setup are presented in Table 9.

Table 8: Pressure field contour plots for a double deck bridge with gap 0.1 m at varying angle of attack



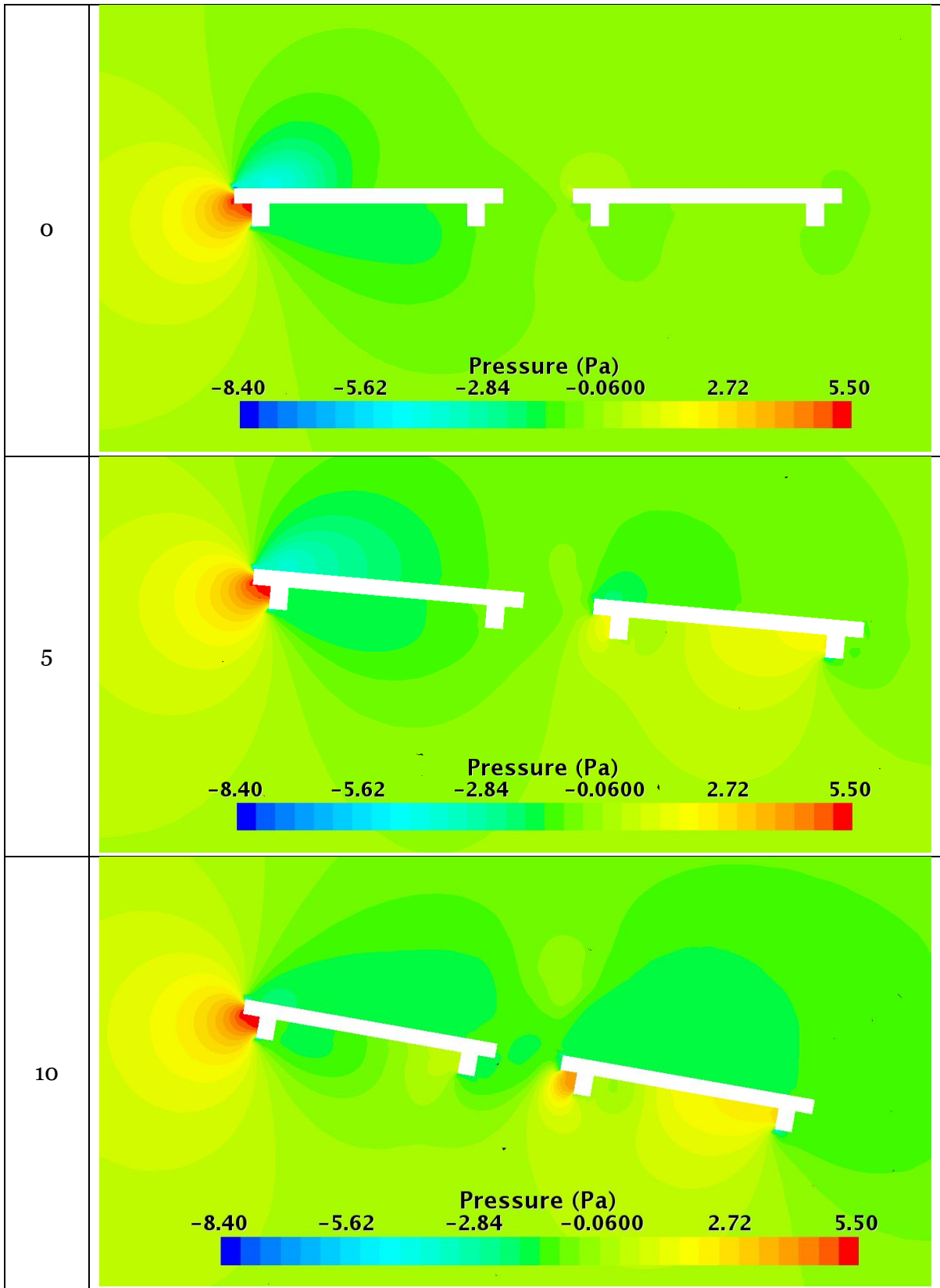
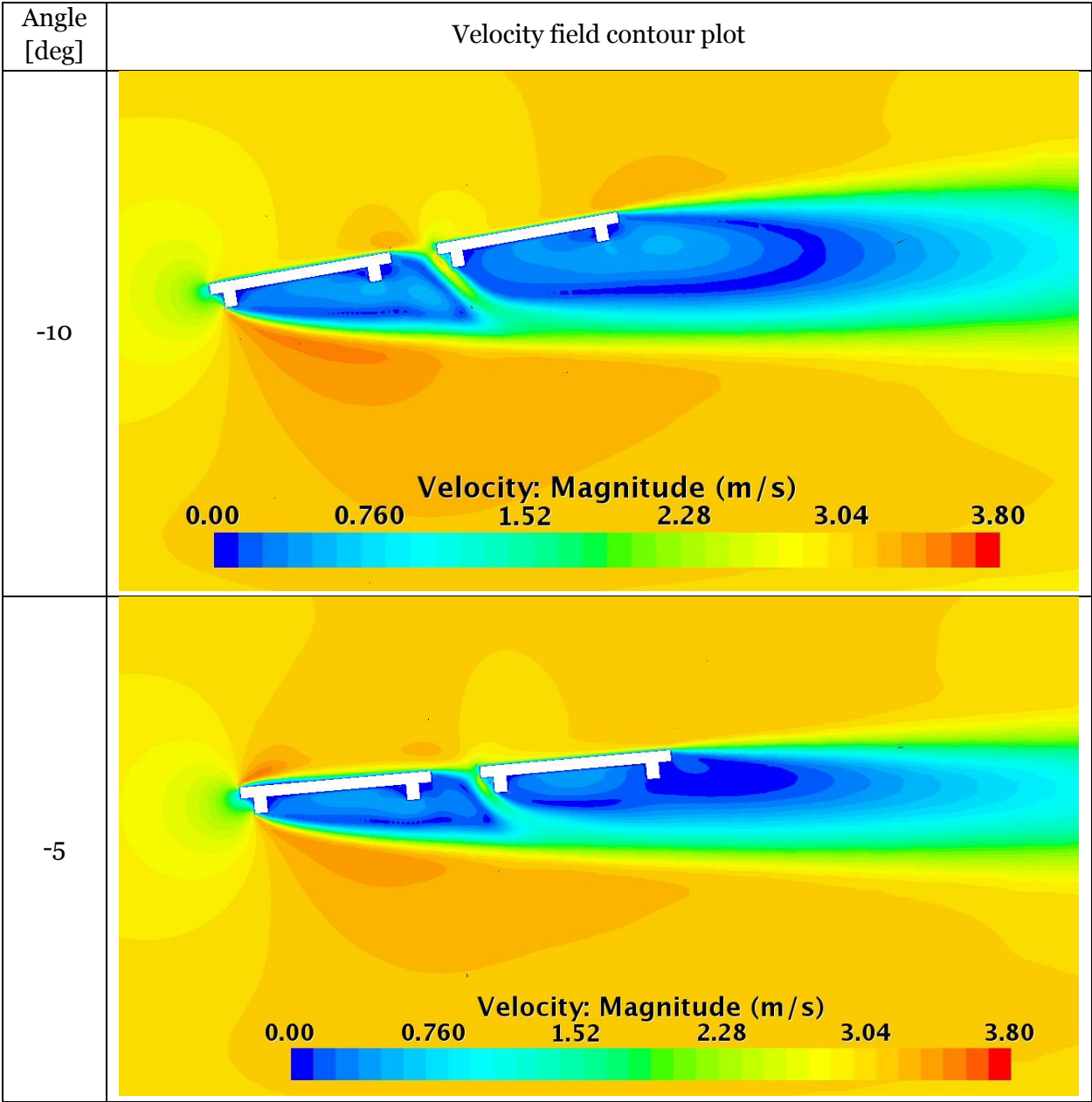
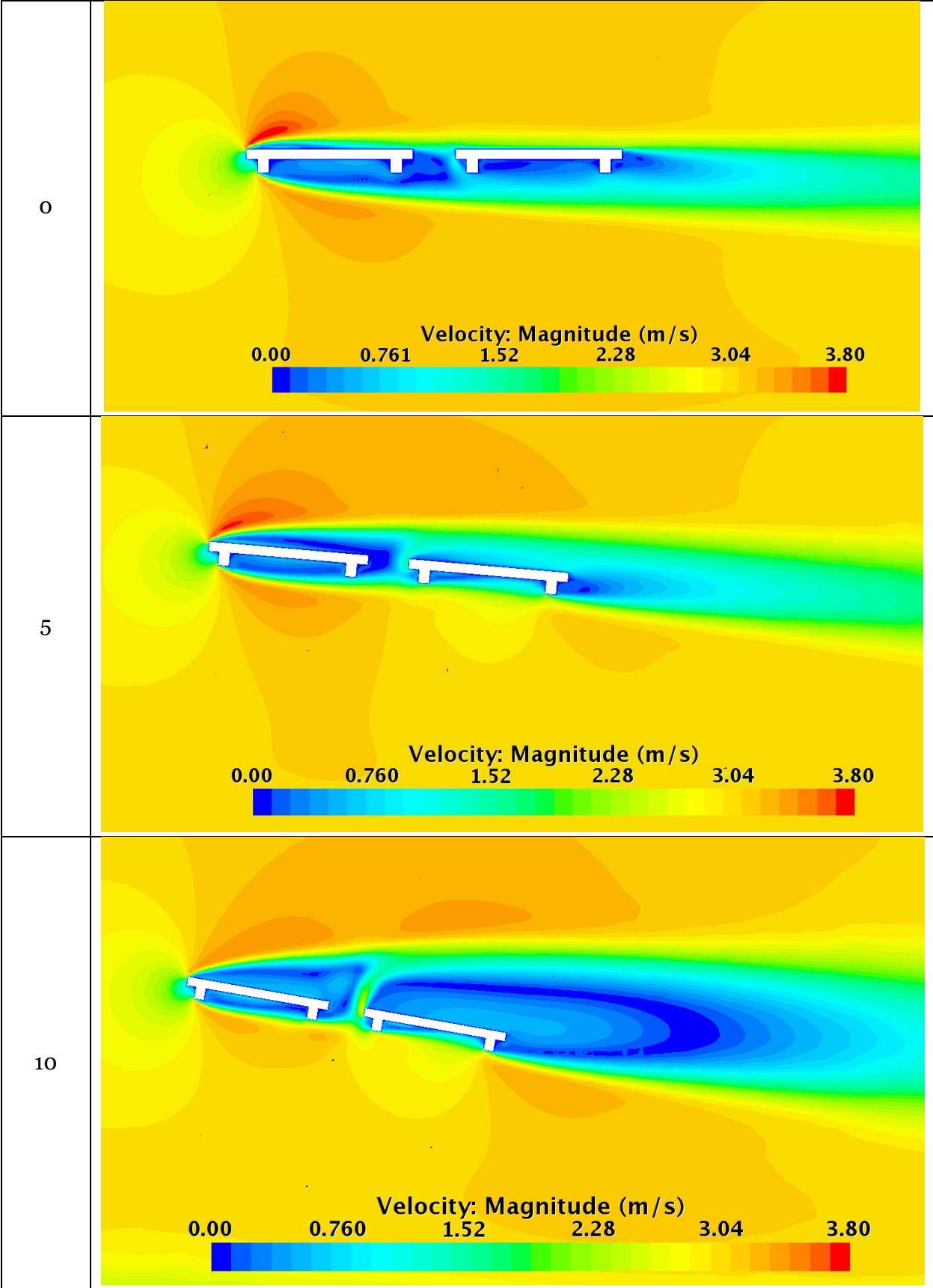


Table 9: Velocity field contour plots for a double deck bridge with gap 0.1 m at varying angle of attack





Maximum and minimum values of pressure acting on decks surfaces, with respect to changing flow direction, are presented in Table 10. Differences in maximum values are not significant with the maximum equal 5.52 Pa at -5 deg angle. The minimum value for a double deck at parallel flow is close to the single deck case and it increases with the increase of the angle of attack. The maximum velocity in the vicinity of the decks doesn't experience big changes and reaches maximum of 3.8 m/s at parallel flow.

Table 10: Extreme values of pressure and velocity for a double deck

Angle [deg]	Pressure [Pa]		Velocity [m/s]
	min	max	max
-10	-6.31	5.48	3.50
-5	-7.11	5.52	3.53
0	-8.38	5.40	3.80
5	-7.45	5.37	3.74
10	-5.21	5.46	3.43

The character of changes of forces due to varying angle of attack is illustrated in Figure 3.13 to Figure 3.15 for a double deck with a 0.1 m distance between decks. Figure 3.13 shows that the character of the curves representing drag forces acting on the decks are similar. The force stays positive and increases with the increase of the angle reaching the maximum of approximately 0.6 N at 10 deg angle. Drag on the upwind deck has similar values to the one deck model for selected flow directions. The biggest difference can be seen for -10 deg angle, where the force equals 0.35 N (as compared to 0.6 N), whereas for 10 deg the values are the closest to each other (and equal approximately 0.6 N). The lift force, displayed in Figure 3.14, changes sign depending on the angle of attack. This tendency is representative for the one deck model as well as for the double deck model. For negative angles of the angle it assumes negative values (the lowest: -0.61 N for deck 2 and -0.736 N for deck 1), goes through zero for angles in the range from -5 deg to 0 deg, and reaches positive values for positive angles. The highest value of the lift force was obtained for the downwind deck at 10 deg angle. It is almost two times higher for the downwind deck than the upwind deck (it is equal 1.5 N for deck 2 and 0.84 N for deck 1) The lift force acting on the single deck at 10 deg angle falls in between these values and is equal 1.1 N. Values of the pitch moment are close to zero for the entire range of flow directions, as indicated in Figure 3.15.

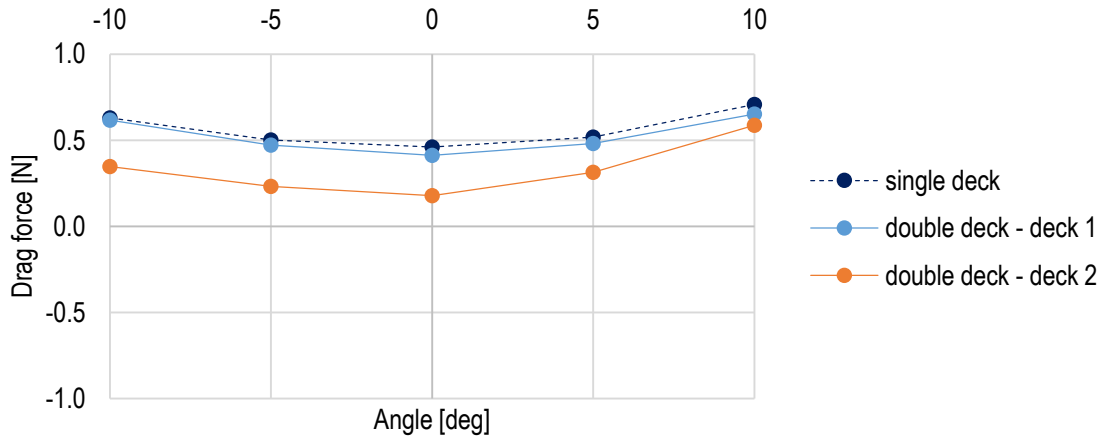


Figure 3.13: Influence of angle of attack on drag force, gap=0.1 m

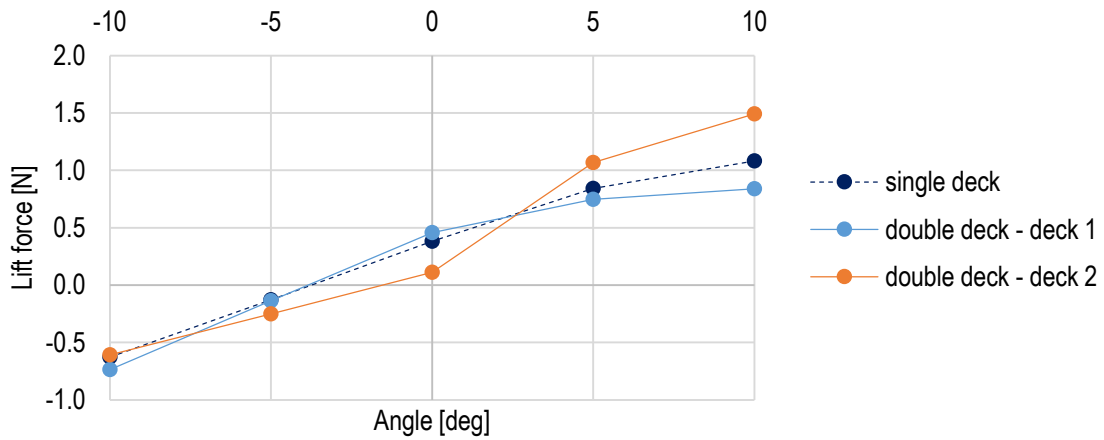


Figure 3.14: Influence of angle of attack on lift force, gap=0.1 m

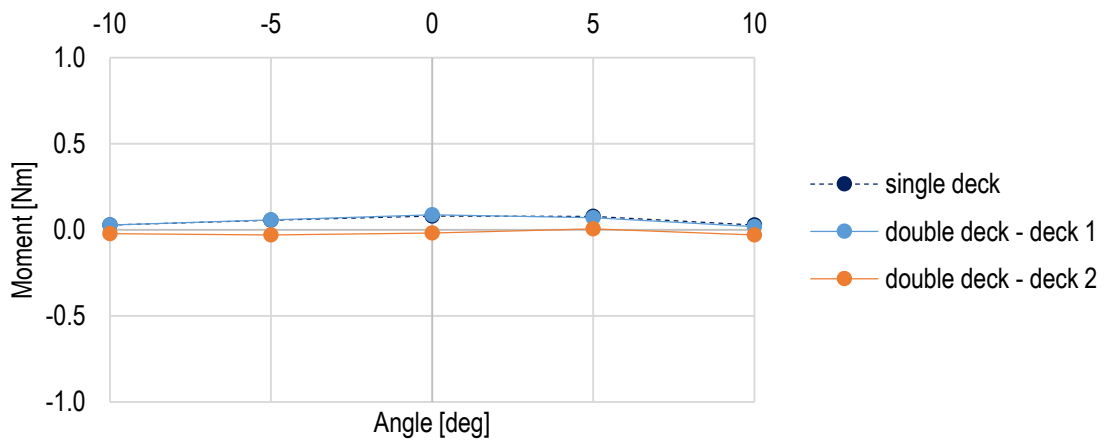


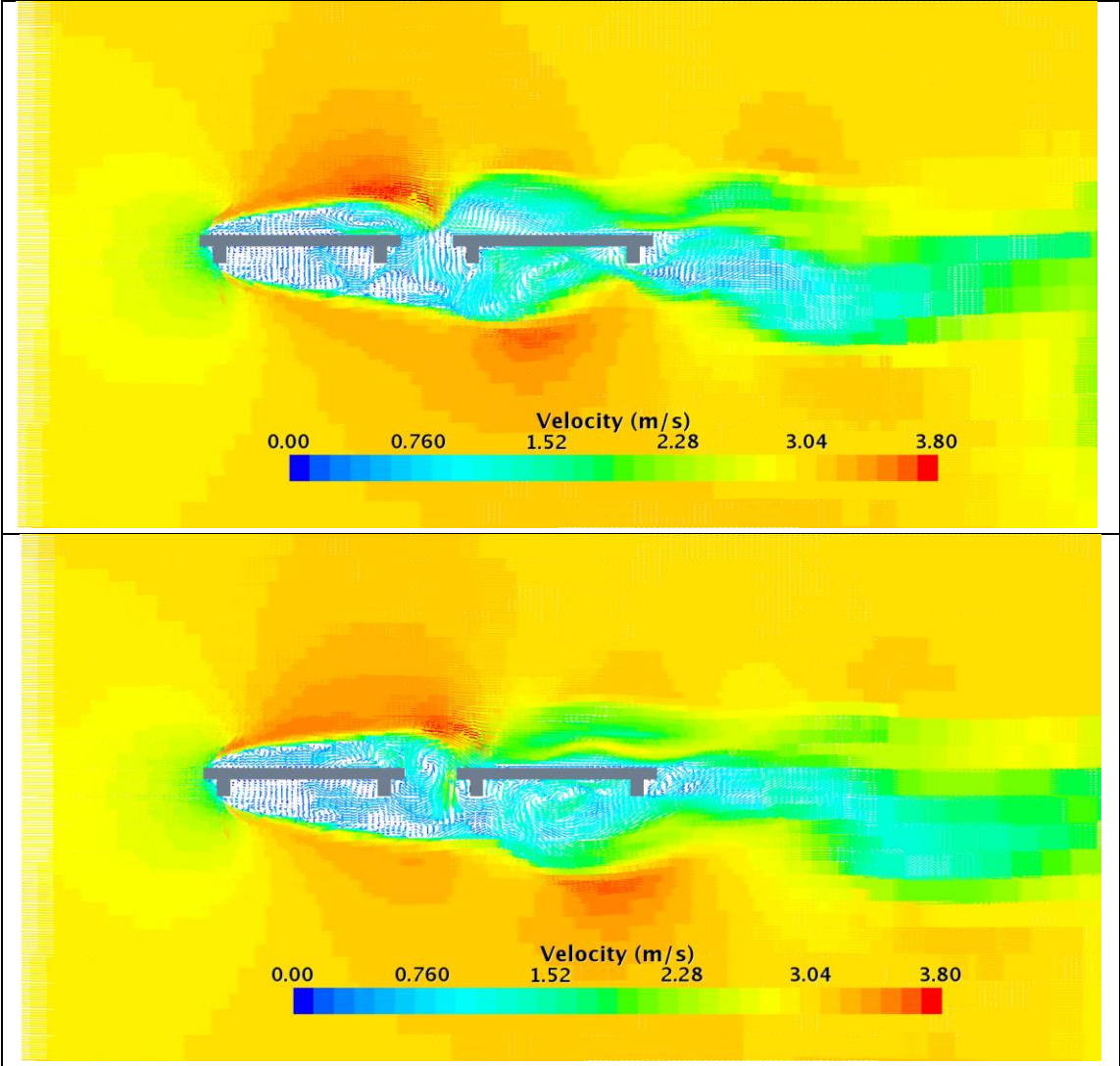
Figure 3.15: Influence of angle of attack on pitch moment, gap=0.1 m

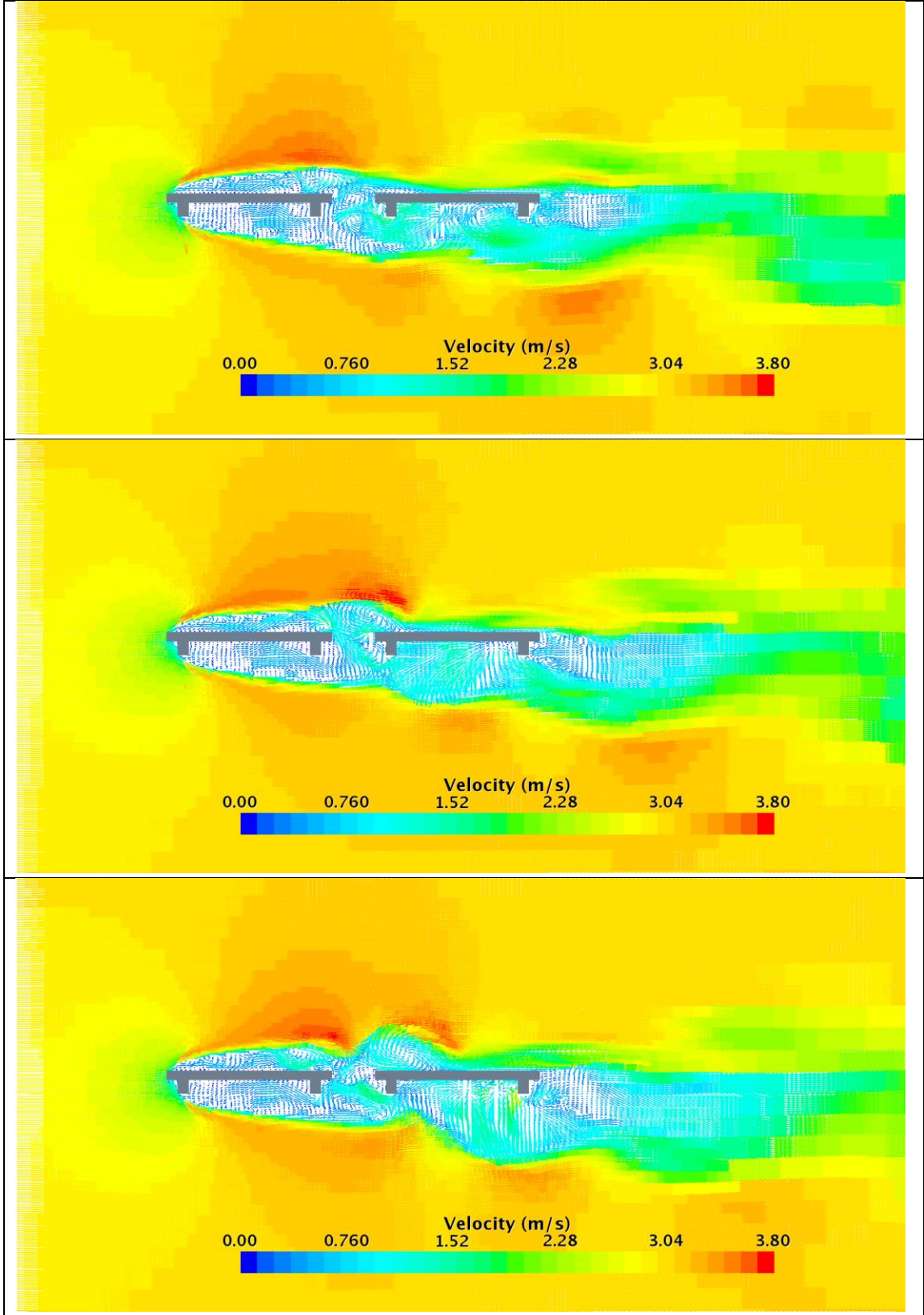
3.4. LES turbulence modeling

LES turbulence modeling was used to capture eddies forming around the stationary decks. The considered cross-section is not streamlined, therefore a formation of vortices is expected around it. The URANS solver with $k-\varepsilon$ turbulence model simulation gives an averaged solution and a smooth and nearly steady flow around the decks, as seen in

Table 7 and Table 9. Table 11 shows a set of images of velocity vector field in consecutive time steps from a LES simulation. The range of velocities is kept constant to better illustrate the field variations.

Table 11: The change in time of velocity vector field around the decks on a plane section





4. Dynamic response

The aerodynamic response of the decks can be investigated with the use of the Dynamic Fluid Body Interaction (DFBI) solver available in Star CCM+. The solver accounts for 6 degrees of freedom of body motion and corresponding mesh morphing as well as fluid transport through the deforming mesh. The URANS solver with the k- ϵ turbulence model was used to solve the fluid flow.

The following model configurations are taken into account and compared:

- decks are stationary
- DFBI configuration 1: both decks are suspended on springs,
- DFBI configuration 2: deck 1 is suspended on springs and deck 2 is constrained,
- DFBI configuration 3: deck 1 is constrained and deck 2 is suspended on springs.

The decks are modeled as rigid bodies, each suspended on 8 springs of assumed length (0.5 m) and stiffness (1000 N/m). Mass, center of mass, and all components of moment of inertia of the deck model have to be provided. These values are obtained using the geometry property computation capabilities of the LS-PrePost preprocessor and an assumed density of the material of 1300 kg/m³. The total mass of a deck equals 20 kg. The center of mass is located 0.015 m under the top surface of the deck. The moments of inertia are: $I_{xx} = 11.6 \text{ kg m}^2$, $I_{yy} = 0.69 \text{ kg m}^2$, $I_{zz} = 12.3 \text{ kg m}^2$. The release time was specified to be 30 sec. The period before the release time allows an initial flow solution to be computed including fluid forces on the deck. After a steady state on stationary decks is achieved, the body suspended on springs is released. The body forces, including fluid forces, can now move the deck. The initial time and the ramp up time (together with the damping forces) should be long enough to reduce sudden non-physical application of the gravitational force to a reasonable level. The deck suspended on springs is allowed to move only vertically and rotate along the centerline of the deck. All other rigid body motions are constrained. The stationary deck is positioned 2.46 cm below the initial location of the moveable deck to take into account the elongation of top springs due to weight of the deck. When the body is released, it moves downwards, pulled by gravity. The displacement oscillates around a constant value with a decreasing amplitude. No structural damping is involved in the simulation, therefore this change is a result of aerodynamic damping.

Force components are recorded for both decks and compared. The forces acting on stationary decks are established during the first 30 sec of the simulation time. Drag force on deck 1 converges to 0.413 N and on deck 2 to 0.178 N. Lift forces converge to 0.455 N and 0.108 N accordingly, and moments to 0.086 Nm and -0.02 Nm.

4.1. Configuration 1: both decks are suspended on springs

Figure 4.1 illustrates DFBI configuration 1, where both decks are suspended on elastic springs. Their vertical motion and rotation are illustrated in Figure 4.2 for the time after the springs are activated. High initial amplitudes, reaching 4.7 cm, decrease in time due to aerodynamic damping. After 100 sec of simulation time they are equal 1.1 mm. Both decks oscillate around the same value of 0.024 m, which is a result of the elongation of the upper springs (and compression

of the lower springs) due to the weight of the model. Amplitude of the motion for the downwind deck is higher than for the upwind deck. Fast Fourier Transform (FFT) was used to establish the vibration frequencies of both decks. The calculations show that the first frequency of the decks is the same and equals 3.14 Hz.

Rotations of the decks are presented in Figure 4.4, where slightly higher values are reported for the downwind deck, with a maximum amplitude of 2 deg, as compared to 1.4 deg for the upwind deck. Rotational frequency is equal to 3.24 Hz.

Forces acting on the decks are combined in Figure 4.5. All quantities converged after 100 sec of simulation time. For the upwind deck they are: drag equals 0.414 N, lift equals 0.462 N and moment 0.077 Nm. The results for a stationary deck are: 0.413 N, 0.455 N and 0.086 Nm, respectively. The differences are smaller for the downwind deck: drag 0.179 N, lift 0.107 N, moment -0.024 Nm (compared to: 0.178 N, 0.108 N, and -0.02 Nm, respectively).

The velocity field is examined in more detail and recorded in the first seconds after the activation of the springs. Table 12 shows how the velocity changes around the decks in consecutive time steps. The velocity vector field is plotted on the middle plane. Table 13 illustrates velocity streamlines changing in time. The seeds for the streamlines lay on the domain inlet at the same height.

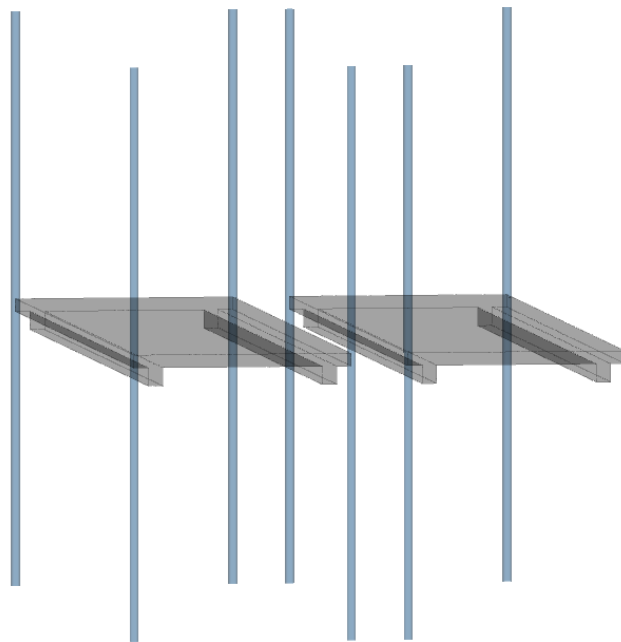


Figure 4.1: Double deck model on elastic springs

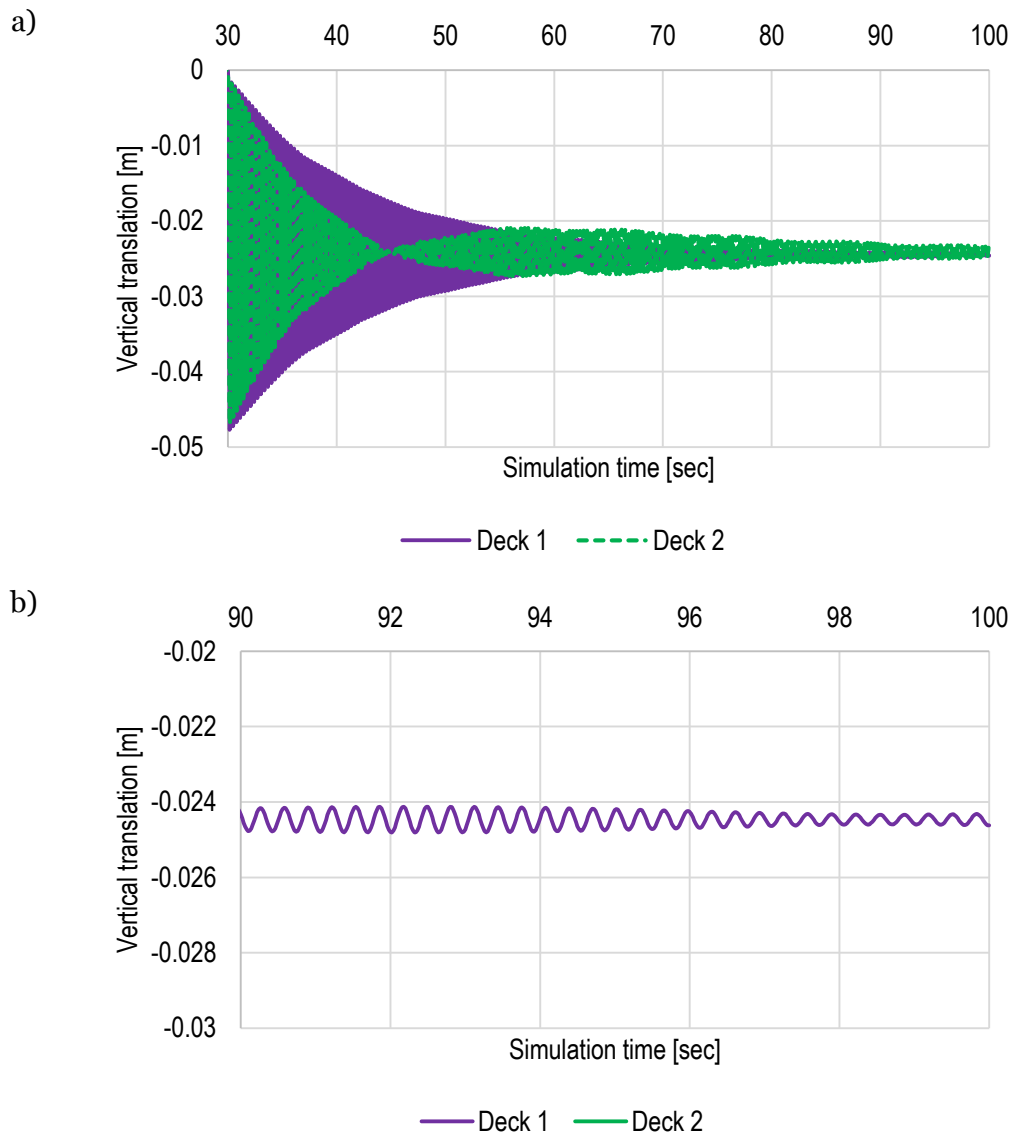


Figure 4.2: Vertical translations of the decks in time, a) during the entire simulation, b) during last 10 seconds of the simulation time.

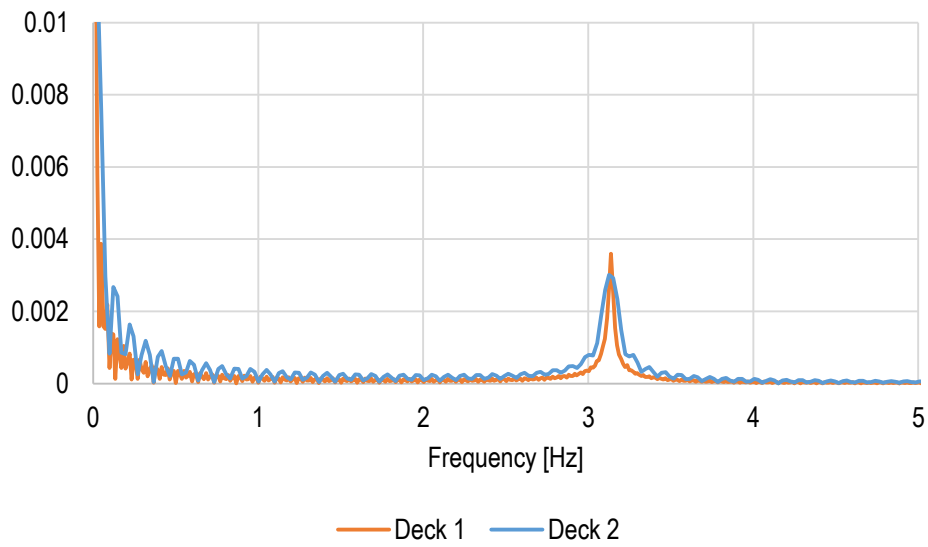
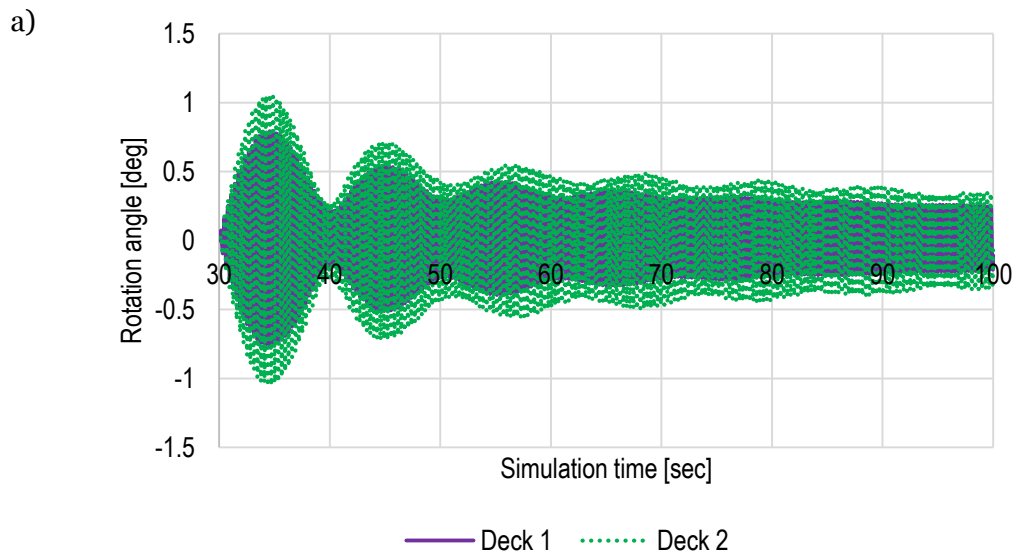


Figure 4.3: Vibration frequencies of the decks



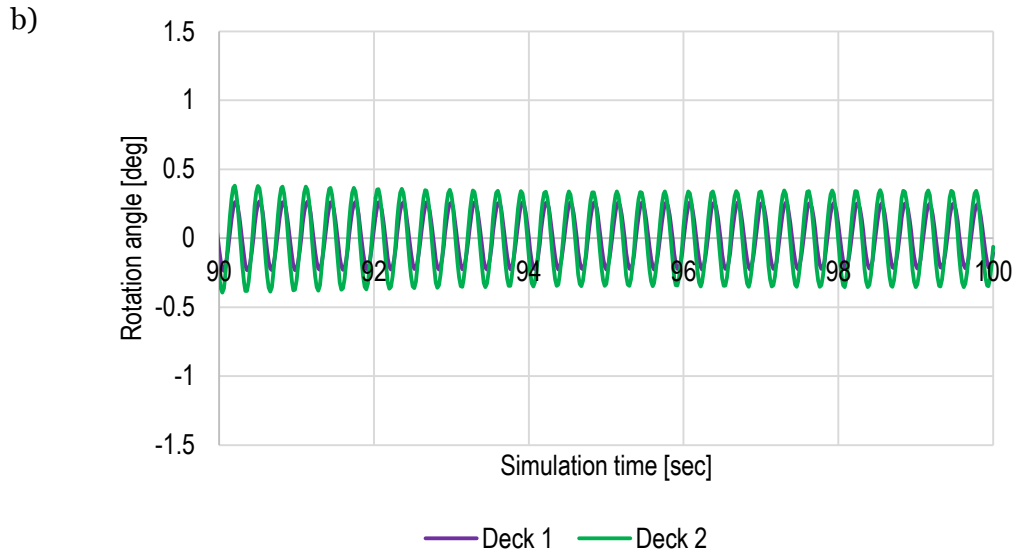
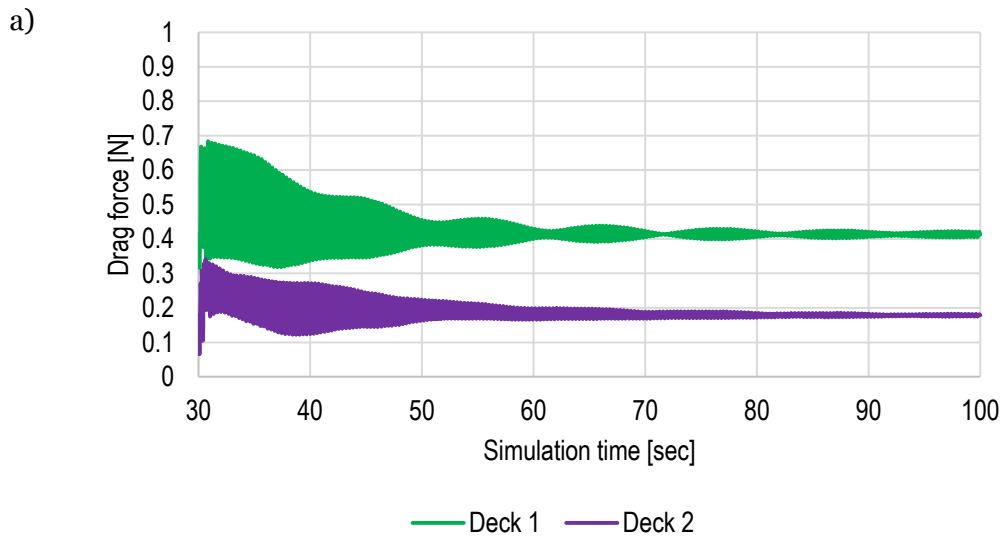


Figure 4.4: Rotations of the decks in time, a) during the entire simulation, b) during last 10 seconds of the simulation time



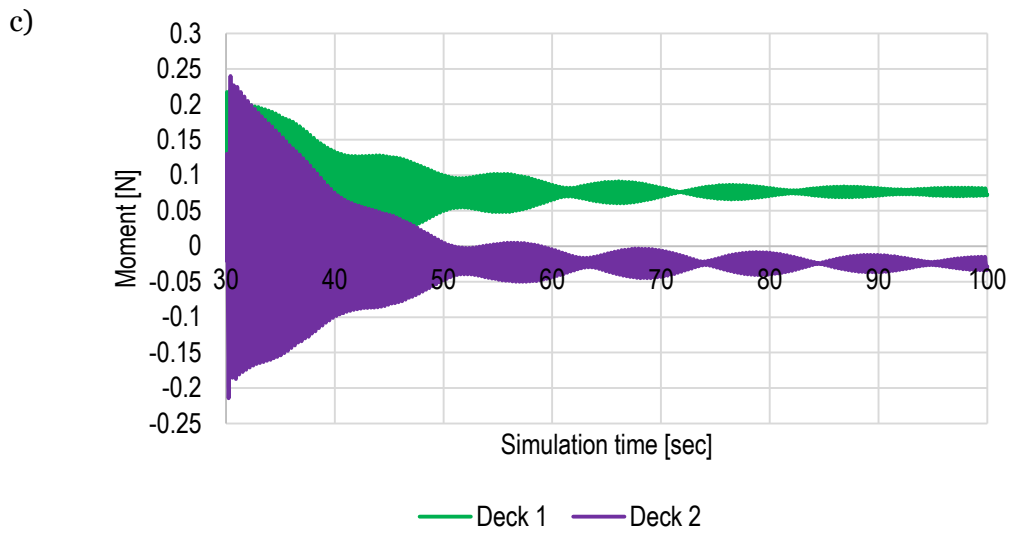
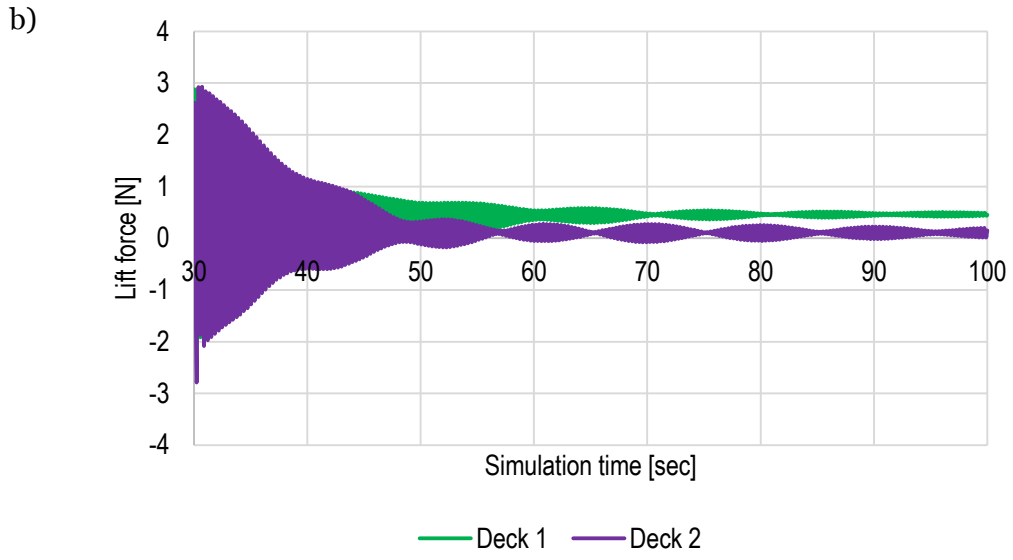
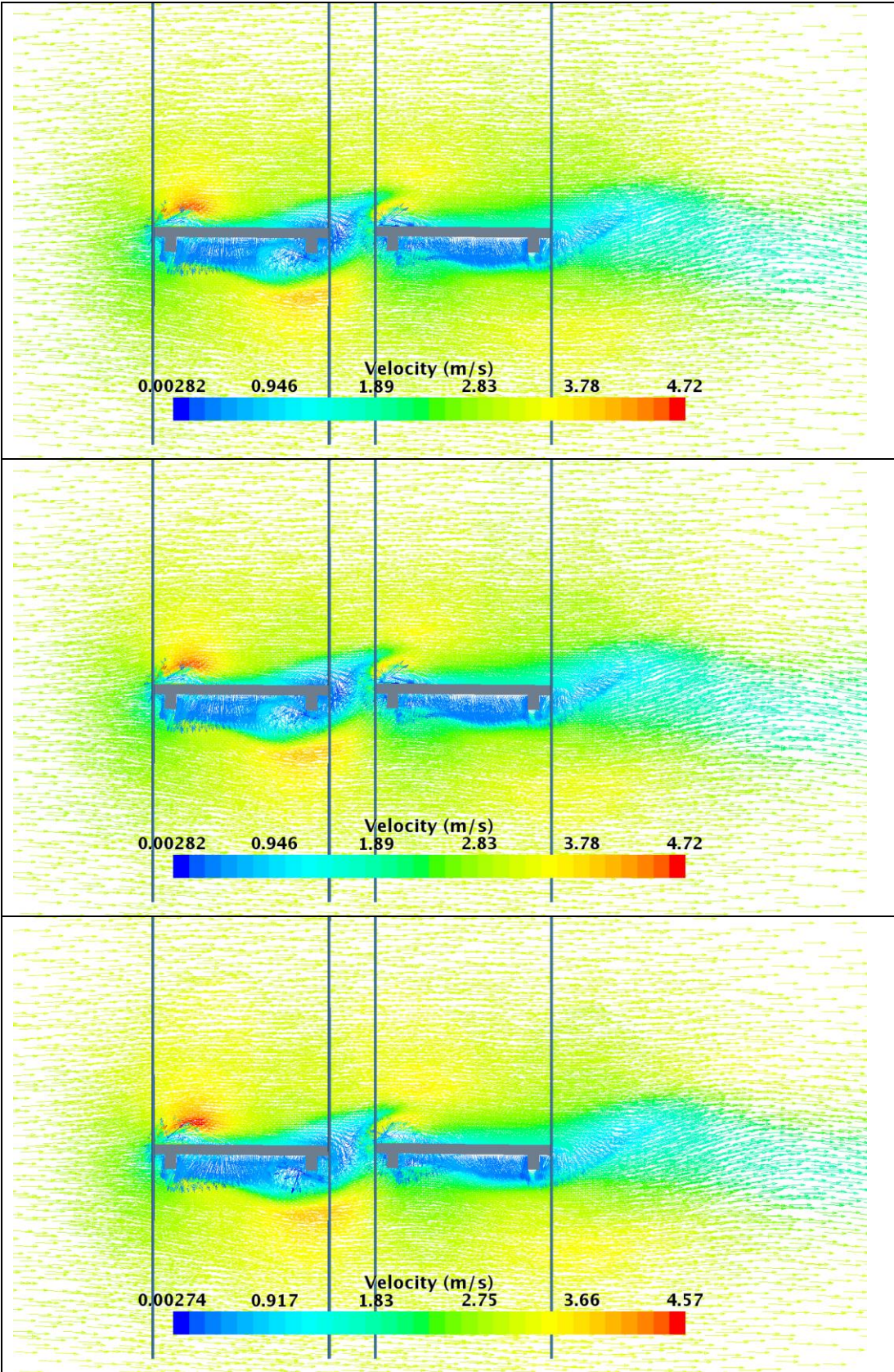


Figure 4.5: Forces acting on the decks in configuration 1, a) drag, b) lift and c) moment

Table 12: Velocity vector field on the middle plane in consecutive time steps



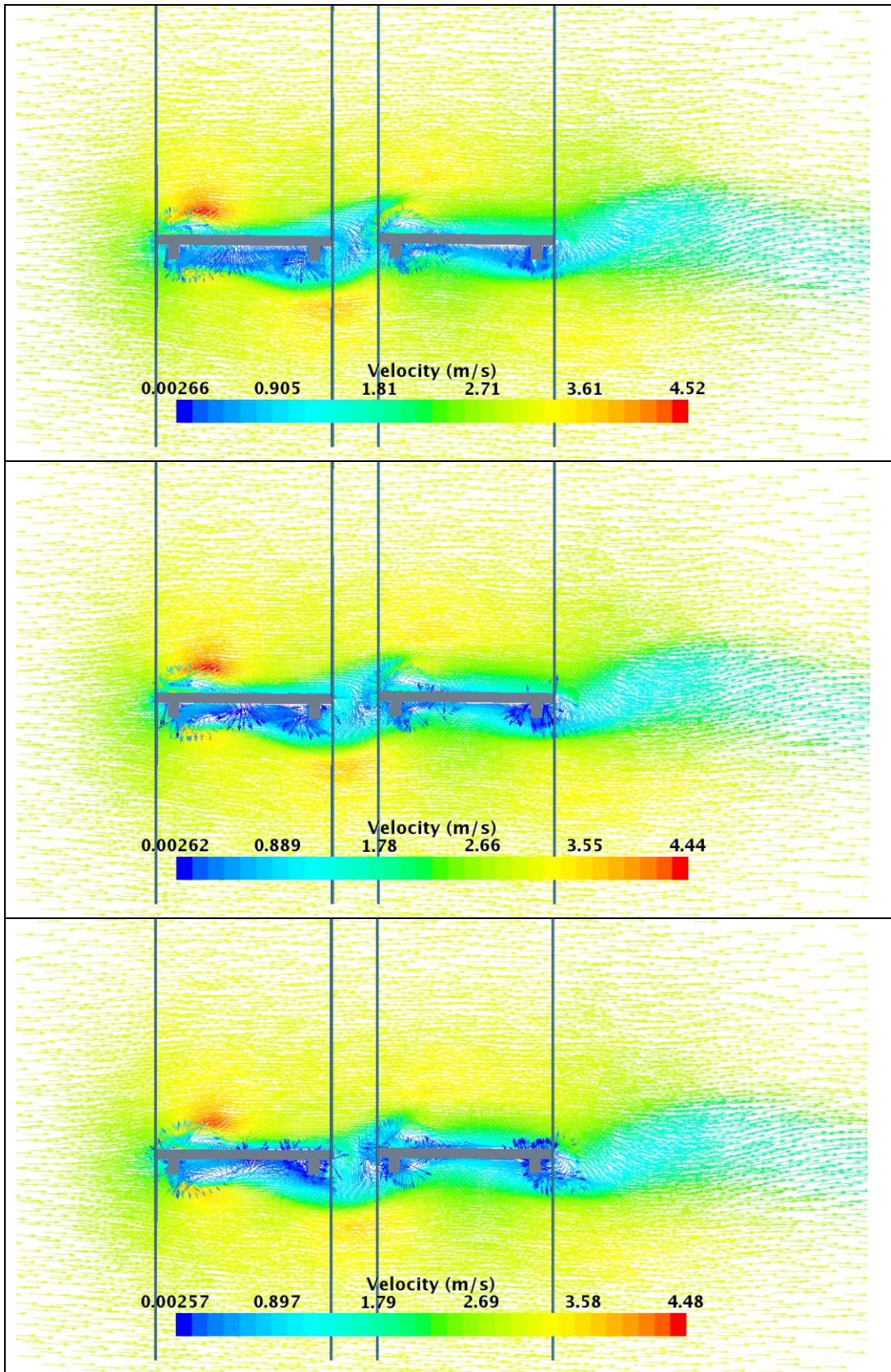
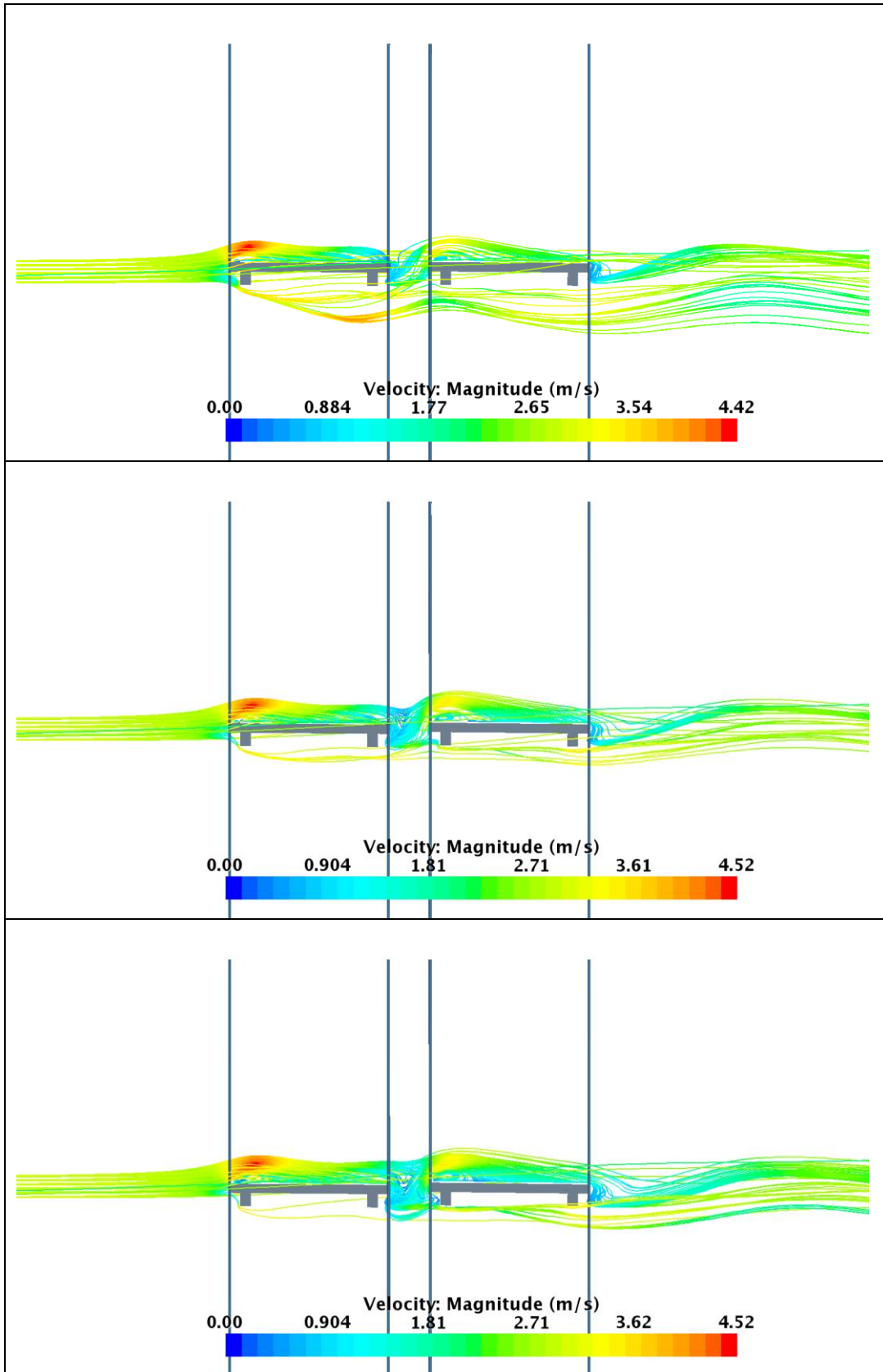
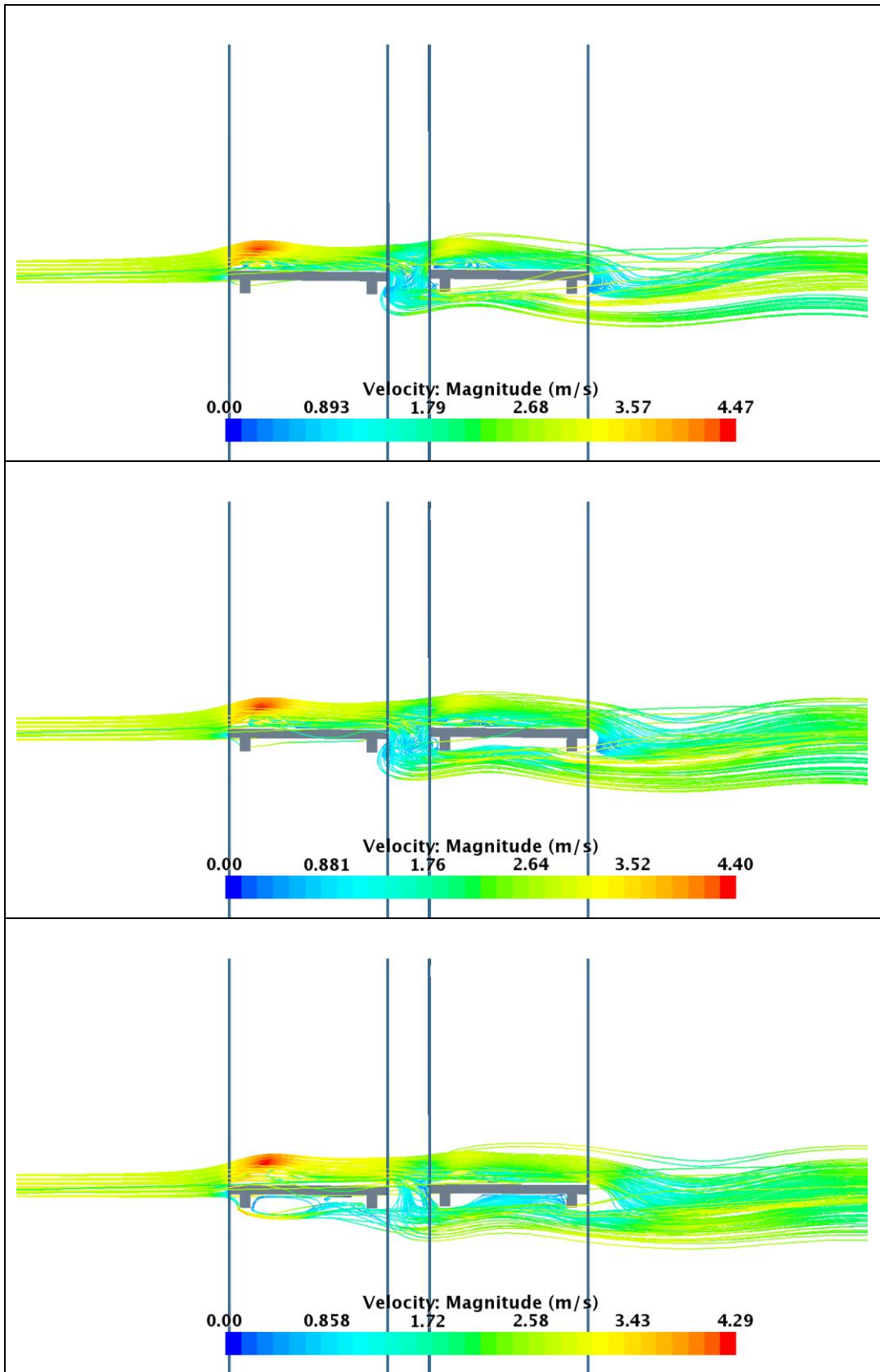


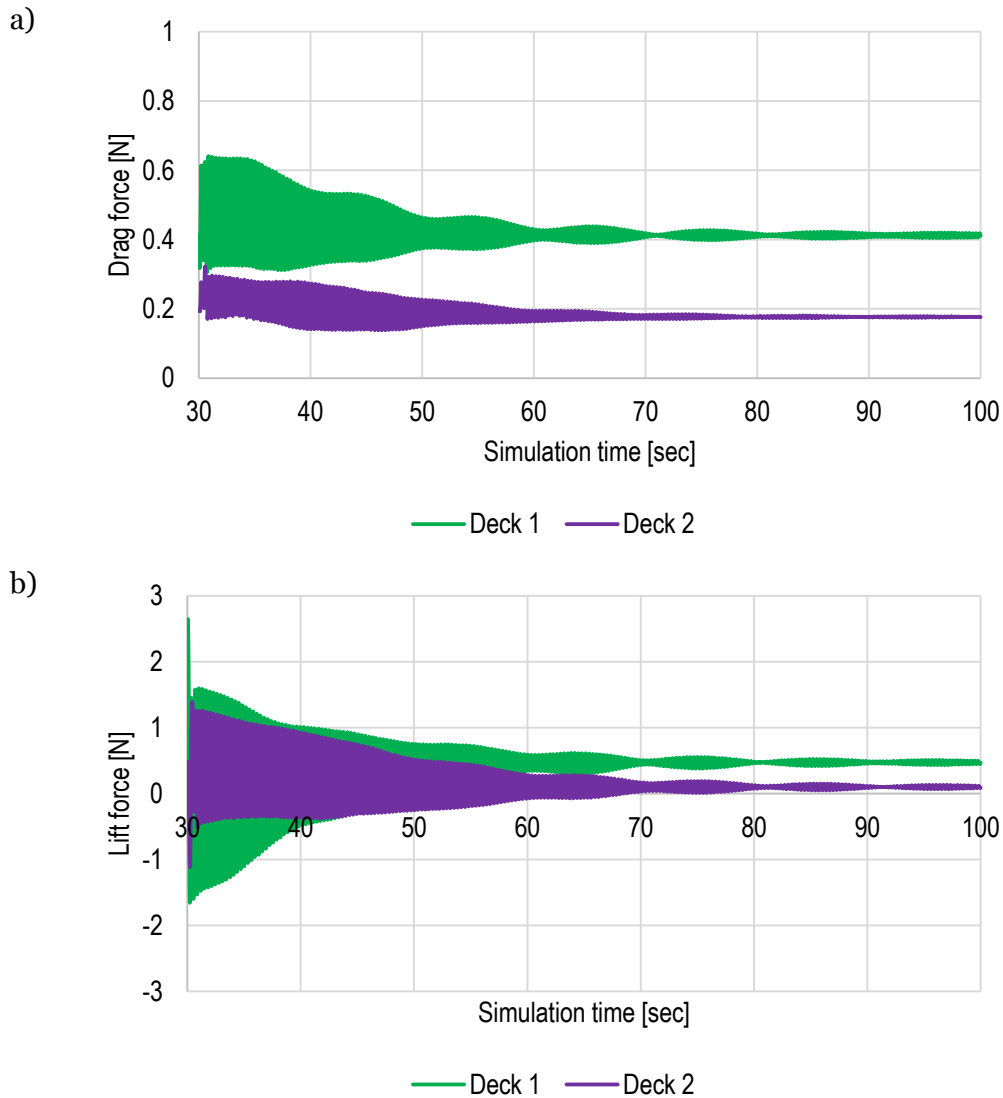
Table 13: Velocity streamlines in consecutive time steps





4.2. Configuration 2: deck 1 is suspended on springs and deck 2 is constrained

In this configuration only the upwind deck is suspended on elastic springs. At the beginning of the simulation it is positioned 0.246 m higher than the downwind deck to take into account the elongation of elastic springs. After the springs are activated, it starts to vibrate in the vertical direction and rotate along the middle axis. The initial amplitude of 4.8 cm quickly decreases to a millimeter and the rotations at the end of the simulation oscillate between -0.238 deg and 0.238 deg. Resultant drag forces, lift forces and moments for both decks are presented in Figure 4.6.



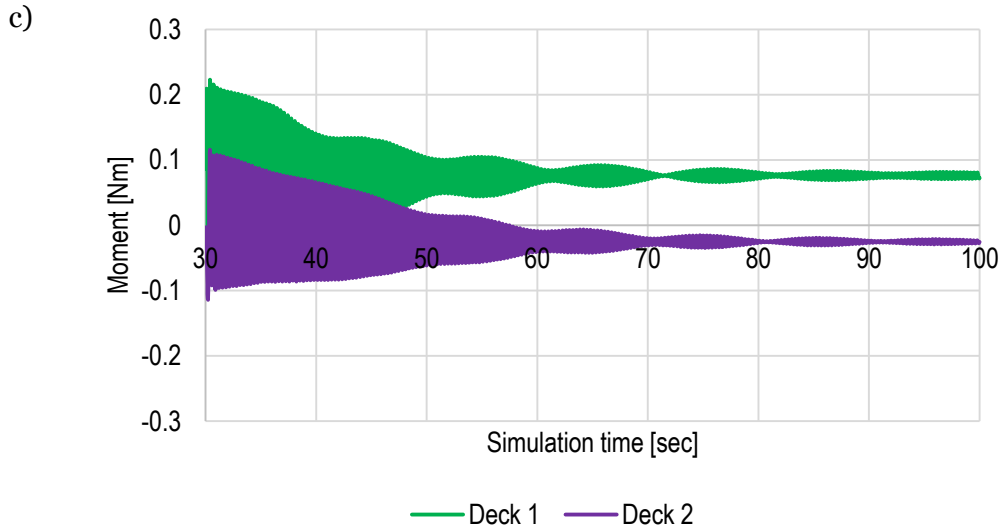
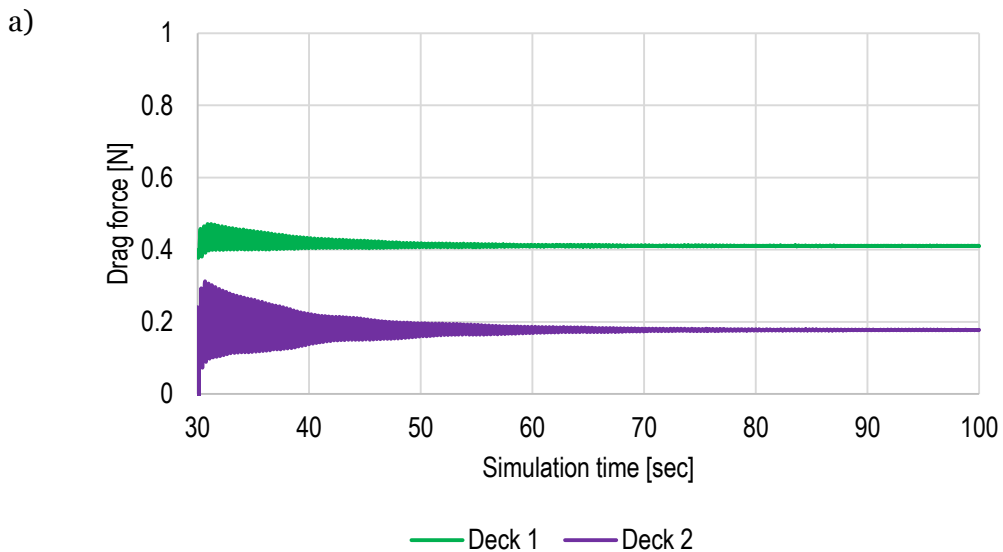


Figure 4.6: Forces acting on the decks in configuration 2, a) drag force, b) lift force, c) moment.

4.3. Configuration 3: deck 1 is constrained and deck 2 is suspended on springs

The force components were also established for a third configuration, in which the upwind deck is constrained and the second is attached to springs, allowing for vertical motion and rotation about the deck center axis. Figure 4.7 summarizes the change of the forces during the simulation.



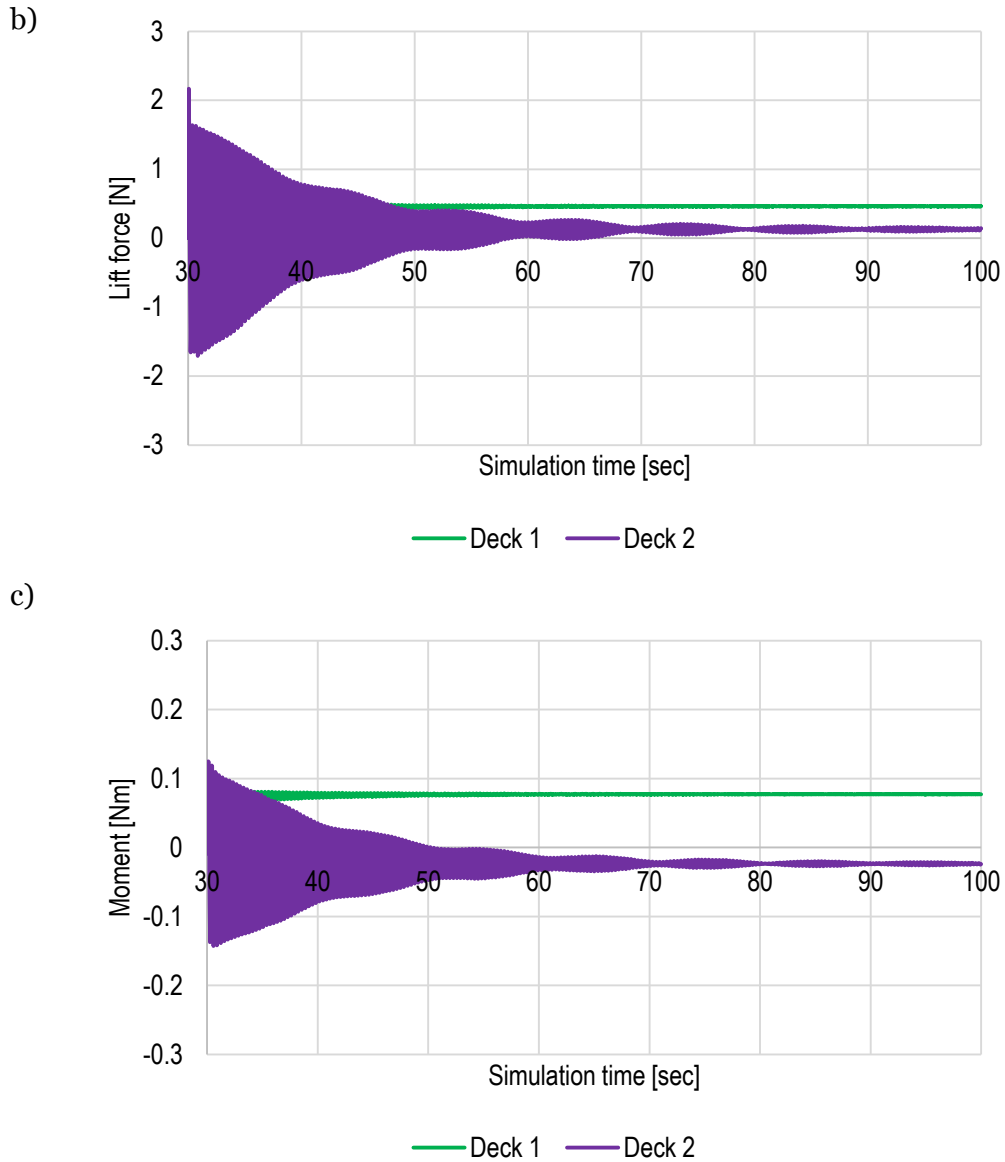


Figure 4.7: Forces acting on the decks in configuration 3, a) drag force, b) lift force, c) moment

4.4. Comparison of results for configurations 1, 2, and 3

Figure 4.8 and Figure 4.9 contain a comparison between the stationary decks model and time averaged force values in three DFBI models. The upwind deck doesn't experience significant changes in forces. The difference in drag forces is small, the differences are less than 2%. The lift forces differ to up to 4%. The differences in moments reach the maximum of 12%. The influence on the forces acting on the second deck are much more pronounced. The drag force stays at the same level, with changes of 1%, but the lift force experiences a change between -7% (configuration 2) to 19% (configuration 3) and the moments – up to 25% of relative error between the base case and the configuration 2.

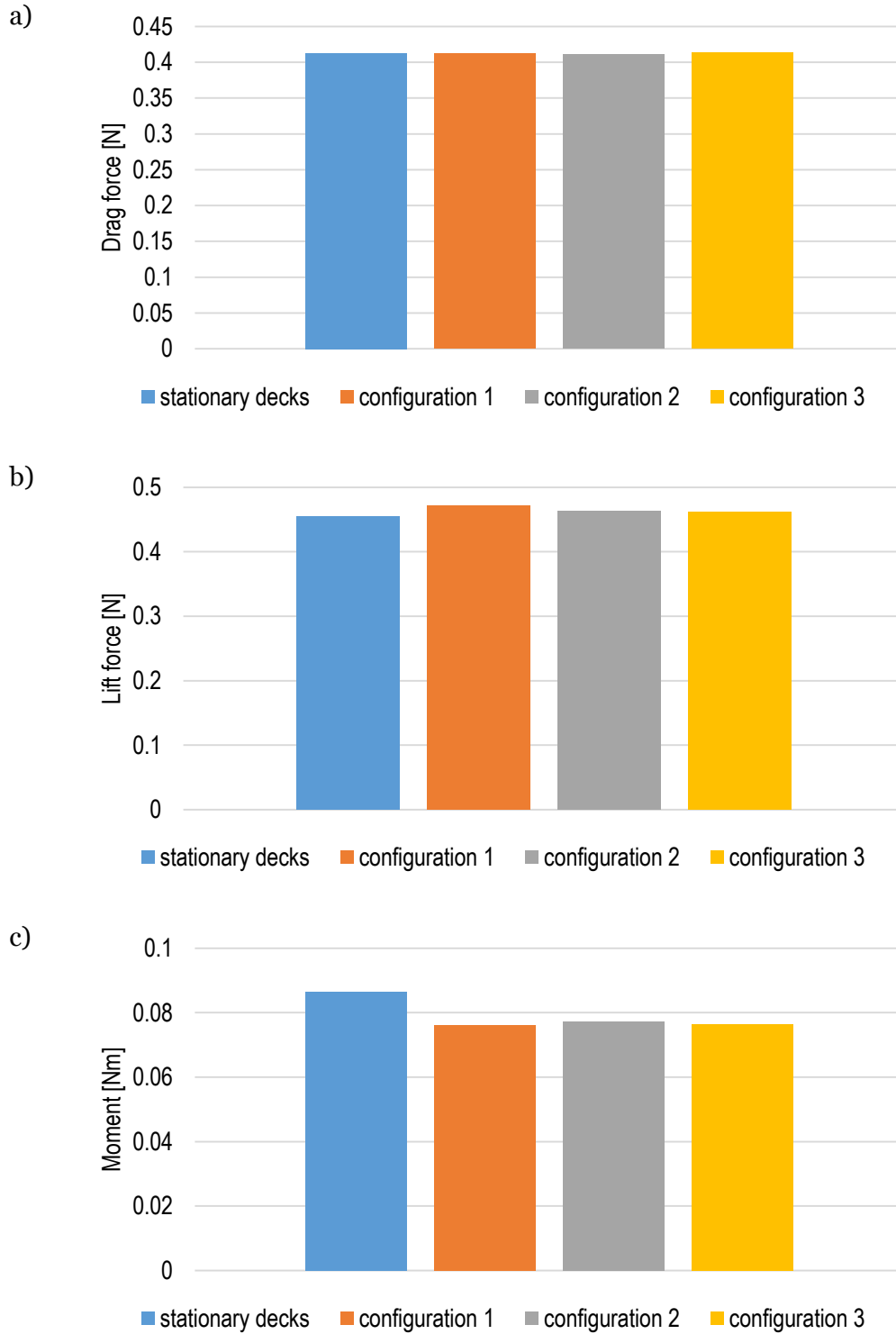


Figure 4.8: Comparison of force values acting on deck 1 at different configurations

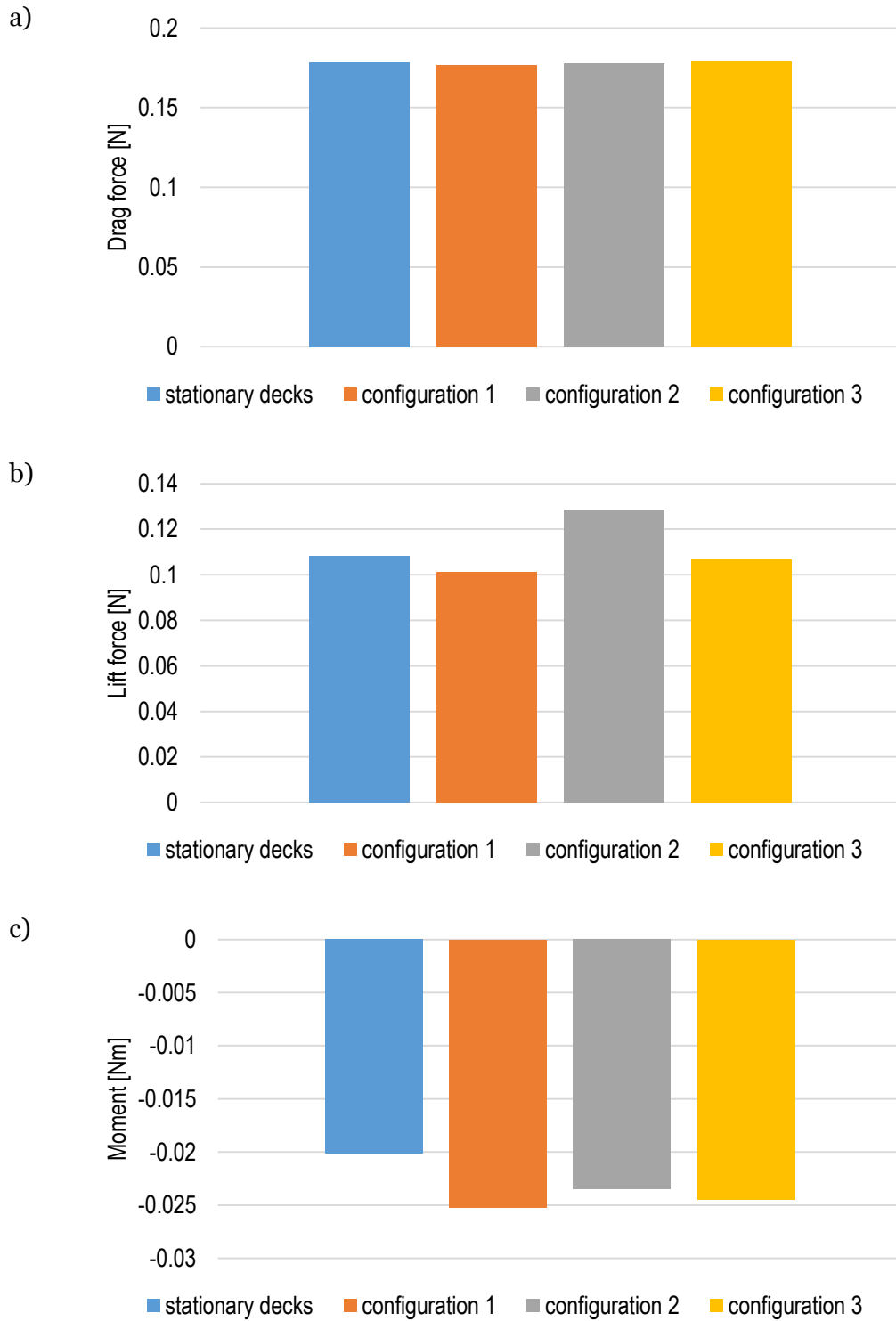


Figure 4.9: Comparison of force values acting on deck 2 at different configurations

5. Conclusions

The main goal of the present study is to assess the capabilities of 3D CFD computations in a parametric study of a twin deck bridge. The aerodynamic loading and response of a rigid section model of generic cross-section was investigated. Gap-to-width ratios, wind speed, and direction were considered using three-dimensional CFD simulations. Static and dynamic responses of the decks were characterized, including computation of steady state aerodynamic forces and pitching moment in RANS as well as LES simulations to capture the formation of eddies.

Mesh density sensitivity tests revealed that there is strong influence on the results depending on the type of the mesh and wall Y^+ value. There are also differences between unsteady URANS solver with $k-\epsilon$ turbulence model and LES computations. A comparison of results led to a conclusion that in static computations it will be beneficial to use URANS and LES models in combination with a polyhedral mesh denser around the decks, so that wall Y^+ is close to unity. Polyhedral meshes are relatively easy and efficient to build and they contain a significantly fewer cells than a hexahedral mesh for the same accuracy. Low wall Y^+ number was chosen to resolve the boundary layer accurately. In dynamic simulations only the RANS model was used to save on computational time and resources.

Single deck simulations were performed in the first stage of the research. The observed pressure and velocity fields serve as a reference for double-deck models. The study shows that forces acting on the single deck model and the upwind deck, regardless of the spacing between decks, have only a small difference in values. The values of lift and moment are higher than for a single deck and they are almost constant regardless the gap size. The downstream deck experiences less drag as it is shielded to some extent by the upwind deck. This effect diminishes as the gap increases. The lift force also increases as the gap gets bigger, but the moments don't vary significantly.

The force change due to varying angle of attack was computed and combined in graphs. The character of the curves representing drag forces acting on both decks are similar. The force is always positive and it increases with the increase of the angle, reaching a maximum at the biggest angle. The lift force changes sign depending on the angle of attack. This tendency is representative for the one deck model as well as for the double deck model. For negative angles it assumes negative values, goes through zero for angles in the range from -5 deg to 0 deg, and reaches positive value for positive angles. The highest value of the lift force was obtained for the downwind deck at the biggest angle. It is almost two times higher for the downwind deck than the upwind deck. Values of the pitch moment are close to zero for the entire range of flow directions.

The aerodynamic response of the decks was investigated with the use of the Dynamic Fluid Body Interaction (DFBI) solver. The URANS solver with the $k-\epsilon$ turbulence model was used to solve the fluid flow. The model configurations that are taken into account are: the decks are stationary, both decks are suspended on springs, deck 1 is suspended on springs and deck 2 is constrained, and deck 1 is constrained and deck 2 is suspended on springs. First two cases are the most common in testing of bridge sections. The following two are usually not considered. Vertical motion and rotation was recorded as well as forces due to the flow conditions. Fast Fourier Transform was used to establish first two frequencies. A comparative study of forces reveals that the upwind deck doesn't experience significant changes in forces, maximum variations are equal a few percent. The influence on the forces acting on the second deck are much more pronounced. The drag force stays

at the same level, but the lift force experiences a change between -7% (configuration 2) to 19% (configuration 3), and the moments – up to 25% of relative difference (between the base case and the configuration 2).

In conclusion, an extensive study was performed on the influence of air flow around a double deck bridge section model. The CFD software used provides an array of features that are useful in aerodynamic simulations, assessment of effects of parameter variation and, visualization of results to gain insight into the flow and pressure around twin bridge decks.

6. References

- [1] Fok, Chin Hong. (2006). "Aerodynamic characteristics of long-span twin-deck bridges." Thesis (M.Phil. Civil Engineering), Hong Kong University of Science and Technology
- [2] Kwok, K. C. S., X. R. Qin, C. H. Fok, *et al.* (2012). "Wind-induced pressures around a sectional twin-deck bridge model: Effects of gap-width on the aerodynamic forces and vortex shedding mechanisms." *Journal of Wind Engineering and Industrial Aerodynamics* 110: 50-61
- [3] Nieto, F., S. Hernandez, I. Kusano, *et al.* (2014). "Assessment of the aerodynamic response of bridge decks by means of 2D Reynolds averaged Navier-Stokes simulations." *10th International Conference on Advances in Fluid Mechanics, AFM 2014, July 1, 2014 - July 3, 2014. WIT Transactions on Engineering Sciences* 82: 407-417, WITPress
- [4] Meng, Xiaoliang, Ledong Zhu, and Zhenshan Guo. (2011). "Aerodynamic interference effects and mitigation measures on vortex-induced vibrations of two adjacent cable-stayed bridges." *Frontiers of Architecture and Civil Engineering in China* 5, no. 4: 510-517



Energy Systems Division

Argonne National Laboratory
9700 South Cass Avenue, Bldg. 362
Argonne, IL 60439-4815

www.anl.gov



Argonne National Laboratory is a U.S. Department of Energy
laboratory managed by UChicago Argonne, LLC